11-2009

MODELING AND SIMULATION OF INTERACTIONS BETWEEN BLAST WAVES AND STRUCTURES FOR BLAST WAVE MITIGATION

Wen Peng

University of Nebraska at Lincoln, wpeng6@huskers.unl.edu

MODELING AND SIMULATION OF INTERACTIONS BETWEEN BLAST WAVES AND STRUCTURES FOR BLAST WAVE MITIGATION

By

Wen Peng

A DISSERTATION

Presented to the Faculty of

The Graduate College at the University of Nebraska

In Partial Fulfillment of Requirements

For the Degree of Doctor of Philosophy

Major: Engineering

Under the Supervision of Professor Zhaoyan Zhang & Professor George Gogos

Lincoln, Nebraska

November, 2009

MODELING AND SIMULATION OF INTERACTIONS BETWEEN BLAST WAVES AND STRUCTURES FOR BLAST WAVE MITIGATION

Wen Peng, Ph.D.

University of Nebraska, 2009

Advisers: Zhaoyan Zhang & George Gogos

Explosions occur in military conflicts as well as in various industrial applications. Air blast waves generated by large explosions move outward with high velocity, pressure and temperature. The blast waves not only incapacitate military and civilian personnel, but also damages buildings, vehicles, and other properties. Hence, there has been extensive research on how to mitigate blast wave effects. Understanding the interactions between blast waves and structures is a very important step in the development of devices for blast wave mitigation. The objective of this dissertation is to explore the complicated physical problem of blast waves impacting structures. The structures comprise flat, V-shaped and cone-shaped structures. The structures can be fixed or free-standing.

It has been recognized that fluid structure interactions (FSI) between a blast wave and a free-standing structure reduces the blast loads exerted on the structure. The dynamic response of a free-standing plate subjected to a blast wave is numerically studied to investigate the effects of FSI in blast wave mitigation. This dissertation develops a 1-D model which includes the blast wave reflection from a free-standing plate,

the plate motion and the shock wave induced in the back of the plate. The Euler equations for the flow fields in the front and in the back of the plate are solved using the Van Leer flux vector splitting scheme coupled with the monotone upstream-centered scheme for conservation laws (MUSCL) and Runge-Kutta scheme.

The reflected pressure for normal reflection is larger than that for oblique and Mach stem reflections, which occur when there is an incident angle between the incident shock front and the reflecting surface. Hence, it is expected that reflected pressure decreases when a blast wave impacts a V-shaped or a cone-shaped structure.

A 2-D numerical model of interactions between a blast wave and a V-shaped or a cone-shaped structure is developed. The model simulates the blast wave reflection from a V-shaped or a cone-shaped structure, the movement of the structure and the induced shock wave behind the structure. Elliptic grid generation and coordinate transformation are utilized to solve the flow fields in the irregular physical domain.

ACKNOWLEDGEMENT

During my doctoral study, I was helped and supported by many people in a variety of ways. I would like to take this opportunity to express my special appreciation.

I would like to express my sincere gratitude and appreciation to my advisors, Professor Zhaoyan Zhang and Professor George Gogos, for providing me with the unique opportunity to work in the research area of blast wave mitigation, for their expert guidance and mentorship, and for their encouragement and support at all levels.

I would like to acknowledge my appreciation to Professor John Barton, Professor David Lou and Professor Ruqiang Feng for their service on my doctoral committee and for their suggestions and reviews of this dissertation.

The research was funded by the U.S. Army Research Laboratory. Their support is gratefully acknowledged.

Finally, I wish to thank my family for their life-long love and support. I especially owe much to my parents, Jinsheng Peng and Liyun Gong, for offering invaluable encouragement to help me overcome difficulties and to make this journey a success.

CONTENTS

LIST OF FIGURES

NOMENCLATURE

Roman

a	speed of sound
e	internal energy per unit mass
e_t	total energy per unit mass
h	thickness
$\vec{n}$	local surface normal
p	pressure
t	time
u	velocity
x, y	Cartesian coordinates
r, y	cylindrical coordinates
C	reflection coefficient
F, $\hat{F}$	flux vector
G, $\hat{G}$	flux vector
I	impulse per unit area
J	Jacobian of transformation
M	local Mach number
R	gas constant
S, $\hat{S}$	source vector

T	temperature
$U,\ \hat{U}$	solution vector
W	blast wave speed and mass

Greek

θ	angle of deflection
β	incident angle
ξ, η	general coordinates
γ	ratio of specific heats
ρ	density
ΔF	difference of force
Δp	difference of pressure

Subscripts

0	initial condition, physical domain
i	incident property, initial property, grid point
g	property of inducted shock wave
p	property of structure
r	property of reflected blast wave
s	property of incident blast wave and Mach stem
u	property of uniform blast wave
v	parameter of inclined surface of a structure
x	parameter in x direction

y	parameter in y direction
ξ	parameter in ξ direction
η	parameter in η direction

Superscripts

*	Intermediate time step
n	time step

CHAPTER 1

INTRODUCTION

1.1 Introduction

Explosions, occurring in military conflicts, send out blast waves of extremely high pressures, which destroy vehicles and incapacitate personnel. With the rise of low intensity conflicts, important structures such as embassies, government buildings become potential terrorist targets. In various industrial applications such as petrochemical, chemical or nuclear industries, there is the potential danger of explosion, which will generate blast waves to damage plant equipment, buildings, and injure civilian personnel. Hence, our understanding and ability to correctly model the complicated physical problem of interactions between air blast waves and structures has important consequences for mitigation of infrastructural damage and human injury.

It has been recognized that fluid structure interactions (FSI) between a blast wave and a free-standing structure reduces blast loads exerted on the structure. Understanding the FSI between a blast wave and a free-standing structure is a very important step in the development of devices for blast wave mitigation. In this dissertation, a structure subjected to a blast wave is treated as a rigid structure and the effects of deformation and stress-wave propagation within the structure are neglected. The basic concept of FSI is that a blast wave impinging on a free-standing structure will cause the structure to recede.

The receding motion of the structure relieves the pressure experienced by the structure and results in a decrease in the impulse transmitted to the structure. Meanwhile, the structure motion induces a shock wave behind the structure, which resists the structure motion. The resistance to the structure motion offsets a fraction of the decrease in pressure experienced by the structure, which is due to the receding motion of the structure. As a result, the impulse transferred to the structure increases, due to the induced shock wave. Both the receding motion of the structure and the resistance to the structure should be considered in the investigation of FSI between a blast wave and a free-standing structure.

Previous work [1-3] on the FSI between a blast wave and a free-standing plate in highly compressible medium has neglected the shock wave induced in the back of the plate caused by plate motion. This assumption leads to over-prediction of the effectiveness of FSI in blast wave mitigation. In another work [4], the effects of incompressible media on both sides of structures were considered for FSI between acoustic waves and structures. Since the blast wave is a shock wave governed by nonlinear wave equations as opposed to an acoustic wave governed by linear wave equations, their simplification results in conclusions that can not be readily applied to blast wave mitigation. To accurately model the FSI between a blast wave and a free-standing plate in highly compressible medium, it is highly desirable to develop a model which includes the shock wave induced by the plate motion. In this dissertation, as a first important step, a 1-D numerical model is developed to simulate the blast wave

reflection from a free-standing plate, the plate motion and the shock wave induced in the back of the plate. The model can be used to predict the effectiveness of FSI in blast wave mitigation, as a blast wave impinges on a free-standing plate.

In general, there are three types of reflection when a blast wave impinges on a surface [5]: (1) normal reflection, (2) oblique reflection, and (3) Mach stem reflection. Normal reflection is the simplest reflection type and occurs when the incident angle is 0°. The incident angle is the angle between the incident shock front and the reflecting surface of a structure. When the incident angle is not 0°, oblique reflection or Mach stem reflection occur. Generally, oblique reflection occurs when the incident angle is less than 40°. Mach stem reflection occurs when the incident angle is greater than 40°. For oblique and Mach stem reflections, part of the reflected wave is diverted sideways. This results in the decrease of the blast loads exerted on the structure.

In order to decrease the reflected pressure, thus reducing the transmitted impulse and improving the blast wave mitigation, V-shaped and cone-shaped structures subjected to blast waves are considered. In this dissertation, as a second important step, a 2-D numerical model and an axisymmetric numerical model are developed to simulate the interactions between a blast wave and a V-shaped or a cone-shaped structure, respectively. The developed numerical models can be used to optimize the design of a structure. A structure can be applied to cover the surface of military or civilian structures to protect against the blast wave impact.

1.2 Literature Review

A considerable number of publications related to interactions between blast waves and structures have appeared in the literature. This dissertation addresses (1) the FSI between blast waves and free-standing structures and the effects of FSI in blast wave mitigation, and (2) the blast wave reflection from structures and the effects of oblique and Mach stem reflections in blast wave mitigation. Therefore, the literature survey will proceed as follows: In the first section, the FSI between blast waves and structures will be discussed. This is followed by a review of the blast wave reflection from structures with various shapes. The last section gives a review of blast wave mitigation strategies.

1.2.1 The FSI between Blast Waves and Structures

In recognition of the advantages of FSI in blast wave mitigation, both numerical and experimental efforts have been devoted to this research area during the past decade. Theoretical and numerical approach is an effective technique to study the FSI between blast waves and structures, and one can avoid the potential dangers associated with handling explosives.

Although FSI problems are characterized by the coupling of the reflected blast wave, the receding motion of the structure and the induced shock wave, some researchers have treated the problem using a simplified approach. Kambouchev et al. [1-3] studied the FSI between a blast wave and a free-standing plate in highly compressible medium, having assumed that a constant atmospheric pressure is applied in the back of the plate and assumed the plate to be rigid. The results show that the impulse transmitted to structures

will decrease with the reduction of the plate mass for fixed blast intensity. Kambouchev [4] also studied the interaction of acoustic waves and structures in incompressible media. The acoustic waves are governed by linear wave equations. The effects of incompressible media on both sides of structures were considered and an analytical solution was derived. Main and Gazonas [6] studied the influence of mass distribution on the uniaxial crushing of a cellular material sandwiched between solid front and back faces, with air blast loading applied to the front face and the back-face unrestrained. An analytical model was developed to investigate the crushing response of the system. FSI effects were treated using the results from Kambouchev et al.[1,2] for air-blast loading on solid plates. It was found that the FSI approximation from Kambouchev et al.[1,2] is inappropriate when the mass of the core is large relative to the mass of the front face, particularly when the decay period of the pressure pulse is comparable to the propagation time of the densification front.

Papers studying the FSI between a blast wave and a flexible structure have appeared in the literature. In this case, the effects of deformation and stress-wave propagation within the structure are considered. With regard to plates, Turkmen and Mecitoglu [7] studied the theoretical analysis of the laminated composite plates exposed to normal blast shock waves and presented correlation between the theoretical analysis and the experimental results of the strain time histories as well. The effects of loading conditions, geometrical properties, and material properties were separately examined on the dynamic behavior. Rudrapatna et al. [8] presented the numerical results for clamped, thin square

plates subjected to blast loading. The nonlinear effects of geometry and material as well as strain rate sensitivity were included. The failure criterion comprising bending, tension and transverse shear was proposed to predict the failure modes. Chafi et al. [9] examined the air-blast simulation using Arbitrary Lagrangian Eulerian (ALE) multi-material formulation. The capability of LS-DYNA was employed to simulate the multi-material ALE formulation and the fluid-structure interaction behavior. The numerical values for parameters, such as the generated peak overpressure, wave arrival time, the deflection of the Rolled Homogeneous Armor (RHA) plate subjected to blast loading were examined with their equivalent experimental values, and good agreements were achieved. Neuberger et al. [10] addressed scaling of the dynamic response of clamped circular plates subjected to blast loadings. The effects of the strain rate sensitivity and variability of material properties with plate thickness on the response of the scaled model were considered. A good agreement between numerical and experimental results was obtained, so that the dynamic response of armor plates subjected to blast loadings can be efficiently modeled and scaled down using geometrical together with Hopkinson's scaling. Alpman et al. [11] simulated the blast loading on a deformable square steel plate, and investigated the effects of coating a steel plate with polyurea. Simulations showed that the polyurea coating prevented fragmentation, but the coating was not very effective for increasing structural stiffness.

With regard to shells, Turkmen [12] studied the dynamic response of cylindrically curved laminated composite shells subjected to normal blast loading theoretically and

experimentally. The effects of material properties on the dynamic behavior were also examined. The strain-time history curves were compared between the experimental and analysis results. Hoo Fatt [13] studied the plastic deformation of a ring-stiffened shell under exponentially decaying pressure load. The structural model give qualitatively correct transient deflections. Redekop [14] investigated the transient blast response of a steel toroidal shell panel under blast loading. Time integration of the equation was performed directly.

The interactions between blast waves and various structures have been widely reported in the literature. Subramaniam et al. [15] investigated blast wave interaction with an elastic structure numerically. The influence of the structural and blast wave parameters on the importance of FSI was studied. It was found that the FSI effect is proportional to the ratio of the structure velocity to the particle velocity of the incident blast wave. Chun et al. [16] investigated the FSI of flexible shelters under blast loading using ANSYS and Fluent. The results were compared with experimental data. It was found that the blast loading and the structural response can not be analyzed separately, due to the FSI between the flexible structure and the blast loading. Therefore, FSI should be considered when the structural deflection rate can influence the solution of the flow field surrounding the structure. Lee et al. [17] studied the blast loads and response of wide flange steel columns under blast loading using finite element program LS-DYNA. The effects of column section size were investigated to estimate the blast resistance of the wide flange section columns. The effects of boundary condition of column ends on

behavior and failure of columns were also observed. Houlston and Slater [18] studied the interaction of air-blast waves with naval panels, which includes the complex structural loading from air-blast wave and the associated structural response. The authors described the method used to couple the ADINA (Automatic Dynamic Incremental Nonlinear analysis) code, which simulates the nonlinear dynamic structural response, with a hydrodynamic air-blast loading code. Two examples associated with the complex pressure loading from multiple reflections of an air-blast wave were presented. Tham [19] studied the interaction of blast waves with a series of aluminum cylinders at near-field, using the fluid-structure coupling feature in AUTODYN-3D. The initial velocities of the aluminum cylinders in the vicinity of the blast field were predicted. The study of the momentum transferred to the cylinders when the explosive charge is initiated at two ends with and without same initiation times was included. Marconi [20] presented a computational investigation of the effects of Rayleigh-Taylor instability on the interaction of the blast wave with a simple structure. The results show that the effects of the instability on the prediction of interaction of a structure and an internal explosion would be significant. Elgy el al. [21] described a series of numerical simulations, conducted using the AUTODYN hydrocode, to compare the effects of detonating an explosive in a mine pot and buried under soil. The subsequent blast and particulate interaction with a structure, the total momentum transferred to a structure and the spatial momentum distribution were investigated for both situations.

The dynamic response of a structure subjected to underwater blast loading is often

substantially different from that under air blast loading. For a structure submerged in a fluid medium, such as water, the FSI problem is characterized by the coupling of the induced fluid oscillations and the resulting motion of the structure. Some of the literature related to the structure subjected to underwater blast loading is also reviewed. McCoy and Sun [22] investigated the dynamic response of a thick-section hollow composite cylinder subjected to underwater blast loading, using finite element analysis and effective modulus theory. The effects of with and without fluid-structure coupling on results were compared. It was found that the effects of fluid-structure coupling are significant. Cichocki [23] applied a nonlinear finite-element computer code ABAQUS to study the effects of underwater explosion in a protective containment structure. The numerical results for various structural configurations of a protective structure were compared. Espinosa et al. [24] proposed a novel experimental methodology which incorporates FSI to assess the dynamic deformation of structures subjected to underwater impulsive loading.

1.2.2 Blast Wave Propagation and Reflection

Papers studying the blast wave propagation and reflection from structures with various shapes have appeared in the literature. Tai et al. [25] discussed blast wave interaction and reflection around closed-ended and open-ended bomb shelters. The Total Variation Diminishing finite volume method was employed to solve the three-dimensional Euler equations. The reflected shock wave patterns transit from regular reflection to Mach reflection in both bomb shelters under an unsteady situation. For

regular reflection, the incident shock wave and the reflected shock wave intersect at the reflection point located on the reflecting surface. For Mach reflection, a Mach stem is formed. The incident shock wave, the reflected shock wave and the Mach stem meet at the triple point. Shi et al. [26] simulated the blast wave interaction with a standalone structural column. Parametric studies included the scaled distance of the blast, column stiffness, and column dimension and geometry. The formula to predict the reflected pressure and impulse on the front and on the rear surface of the columns with different dimensions and geometry were derived. Yang et al. [27] numerically studied the shock wave reflection patterns generated by a blast wave impinging on a circular cylinder. The transition from regular to Mach reflection, trajectory of the triple point, and the complex shock-on-shock interaction were discussed. Blast wave propagation and reflection has also been investigated experimentally. Takayama and Sekiquchi [28] studied the interaction of a spherical shock wave with a planar or conical wall. The shock wave was induced by expanding a planar shock wave into free space in a conventional shock tube. When a spherical shock wave encounters a planar or conical wall, a transition from regular to Mach reflection takes place with the incident angle larger than the critical transition angle. Dewey and McMillin [29] used high speed photogrammetry to investigate the blast wave interaction with ideal and real surfaces. It was observed that a smooth surface induces a stronger Mach stem.

Blast wave reflection from plates has been investigated. Liang et al. [30] studied the transition behavior of an unsteady cylindrical blast wave reflection from a flat plate. For

the first outward-moving shock wave which is followed by expansion waves, the type of reflection transits from the regular reflection to Mach reflection. However, for the secondary shock-wave which is induced by the expansion waves, the type of reflection remains the regular reflection. Later, Liang et al. [31] calculated a strong spherical blast wave interacting with a flat plate to study the blast wave reflection from a flat plate and the associated flow structure. It was found that near the flat plate there are at least three local high-pressure regions behind the curved Mach stem. Colella et al. [32] numerically studied the two-dimensional axisymmetric reflection of a spherical blast wave from a plate, which creates complex flow structures on multiple length scales.

Blast wave reflection from wedges has also been investigated, both numerically and experimentally. Olejniczak et al. [33] numerically studied the steady inviscid shock interactions on double-wedge geometries. The effects of varying second wedge angle and Mach number on the phenomena of interaction were discussed. Five interaction types and the transition criteria between the various interactions were identified. Ben-Dor [34] simulated the reflection process of a planar shock wave over concave and convex double wedges. The pressure distributions along the two surfaces of the double wedge were investigated, and the points along the double wedges that are subjected to the highest and lowest pressures were revealed. Igra et al. [35] numerically studied the reflection process of a traveling wave from a wedge placed in various suspensions. The reflection process from the deflecting wedge was studied for different dust mass loadings and different dust particle diameters. It was shown that the dust loading and dust particle diameter affect the

wave reflection pattern. It was also shown that the dust presence affects the pressure on the wedge surface significantly. Igra et al. [36] investigated blast wave reflection from wedges experimentally and numerically. In the numerical study, the two-dimensional Euler equations were solved using a Godonuv based, second-order accurate scheme. A shock tube equipped with a very short driver was employed for the experiments. The reflected wave pattern is similar for the interaction of a blast wave or a shock wave with a wedge when both incident waves have the same initial pressure jump across their fronts, but the resulting pressure field is different. Takayama et al. [37] investigated the transition of regular reflection and Mach reflection over concave and convex, smooth and rough wedges experimentally. It was revealed that as the surface roughness increases, the wedge angle at which transition takes place (for a given Mach number) decreases.

1.2.3 Blast Wave Mitigation Strategies

Many approaches have been used to protect the structures, such as providing a blast barrier, applying the FSI concepts to structural designs like sandwich constructions, using energy-absorbing materials like metal foams, porous shape memory alloys, and laminated glass, etc.

One simple way of enhancing the survivability of structures to blast loads is to provide a blast barrier at the perimeter [38]. Rose et al. [38-39] measured the blast environment behind a blast wall in scaled tests. Comprehensive contour plots of overpressure and impulse behind the blast wall were developed. It was found that a blast wall can effectively protect buildings against air blast wave from high explosives. Blast

walls constructed from a range of materials, including plain sand monoliths of different thickness, sand enclosed in scaled geotextile materials, wood, expanded foam plastic and water, were tested in their later work [40]. It was found that, for the rapid provision of protection, non-permanent structures can provide a high degree of blast wave attenuation. Zhou and Hao [41] carried out numerical simulations to study the effectiveness of blast barriers for blast load reduction. The results show that a blast barrier not only reduce the peak reflected pressure and impulse on a building behind the blast barrier, but also delay the arrival time of the blast wave. An approximate formula was derived to estimate the reflected pressure-time history on a building behind a blast barrier.

Su et al. [42] employed the FSI concepts to propose a novel blast wave mitigation device, consisting of a piston-cylinder assembly. A shock wave is induced inside the device when it is subject to a blast wave. The essence of their blast wave mitigation device is to reduce a high-pressure short-duration impact to a low-pressure long-duration impact. The effectiveness of the blast wave mitigation device was studied numerically. It was found that the transmitted impulse remains practically unchanged, while the peak pressure of the blast wave can be reduced by as much as 98%.

The FSI concepts have the potential to be applied to structural designs, such as sandwich panels made of various materials and core topologies. The general core materials include polymer foams, metal foams, and metal honeycomb, etc. The interaction between blast waves and sandwich structures to develop blast-resistant materials and structures has been studied. Qiu et al. [43-45] investigated the sandwich

plates with cellular cores. An analytical model was developed to describe the deformation of sandwich panels subjected to shock loading. It was suggested that the response of sandwich structures can be separated into three sequential stages: 1) FSI phase, 2) core compression phase, and 3) plate deflection and stretching phase. Therefore, the sandwich plates have a higher shock resistance than monolithic plates of equal mass. Vaziri and Hutchinson [46] exploited the results of Kambouchev et al.[1] to assess the performance of all-metal sandwich plates compared to monolithic solid plates of the same material and mass per area. Square honeycomb and folded plate core topologies were considered. The results show that square honeycomb cores perform better than folded plate cores due to their ability to maintain a high crushing strength at relatively large crushing strains. Xue and Hutchinson [47, 48] performed highly refined three-dimensional finite element simulations to assess the performance of metal sandwich plates subjected to impulsive blast loads. The examples studied demonstrate that there is considerable potential for exploiting metal sandwich plate construction for blast resistant structures. Sandwich plates with sufficiently strong cores are capable of sustaining larger impulse than solid plates of the same material and weight. The specific examples considered in these papers substantiate that fluid structure interactions enhance the performance of sandwich plates relative to solid plates under intense air shocks, but not as significantly as for water blasts. Wang et al. [49] studied the blast resistance and energy absorption of sandwich composites with a stepwise graded foam core when experimentally subjected to a shock wave loading. Two types of core configurations, with identical core materials but

different core layer arrangements, were investigated. Configuration 1 consisted of low/middle/high density foams and configuration 2 consisted of middle/low/high density foams. The shock pressure profiles and real time deflection images were analyzed to reveal the failure mechanisms of the sandwich composites. The overall performance of configuration 1 was better than that of configuration 2. Qiao et al. [50] presented a review of impact mechanics and high-energy absorbing materials. Some developments in numerical simulation of impact and new design concepts proposed as high energy absorbing materials (lattice and truss structures, hybrid sandwich composites, and metal foams, etc.) were discussed. Impact damage on composite materials in aerospace engineering was discussed as well.

The dynamic response of sandwich structures subjected to underwater blast loading has also been investigated. Liang et al. [51] examined the response of metallic sandwich panels to the impulse caused by underwater blast. Three core topologies (square honeycomb, I-core and corrugated) were used to address fundamental issues affecting panel design. The results were compared with analytic solutions based on a three-stage response model and provide insights into the design of optimal panels. Fleck and Deshpande [52] studied the blast resistance of clamped sandwich beams under air and underwater blast loading. The structural response of the sandwich beam was split into three sequential steps. Performance charts for a wide range of sandwich core topologies were constructed to find an optimal design. Tilbrook et al. [53] used finite element calculations to study the dynamic response of sandwich beams subjected to underwater

blast loading. The effects of fluid structure interactions were included. The results indicate that appropriately designed sandwich beams undergo significantly smaller back face deflections and exert smaller support forces than monolithic beams of equal mass.

1.3 Dissertation Outline

This dissertation is organized as follows. Chapter 2 presents the dynamic response of a free-standing plate subjected to a blast wave. The flow fields on both sides of a free-standing plate are modeled using 1-D Euler equations. A 1-D numerical model is developed, which includes the blast wave reflection from a free-standing plate, the plate motion and the shock wave induced in the back of the plate. The numerical model is validated in two parts. The first part is to validate the model for the flow field in front of the free-standing plate. The numerical results, which are obtained by assuming a constant atmospheric pressure in the back of the plate, are compared with the numerical results available in the literature. The second part is to validate the model for the flow field in the back of the free-standing plate. The numerical results for a free-standing plate with a constant velocity are compared with analytical solutions available in the literature. The numerical results obtained from the integrated model are discussed to investigate the effects of FSI in blast wave mitigation. Both uniform and exponential blast waves are simulated.

Chapter 3 investigates the interactions between a blast wave and a V-shaped or a cone-shaped structure. The flow field in front of a V-shaped structure is modeled using

2-D Euler equations in Cartesian coordinates. The flow field in front of a cone-shaped structure is modeled using 2-D Euler equations in cylindrical coordinates. The flow field in the back of a structure is modeled using 1-D Euler equations. A 2-D numerical model of interactions between a blast wave and a V-shaped or a cone-shaped structure is developed and validated by comparing the numerical results with the analytical solutions available in the literature. The numerical model is used to investigate the effects of FSI coupled with oblique or Mach stem reflection in blast wave mitigation. Both uniform and exponential blast waves are simulated.

Chapter 4 and chapter 5 present the concluding remarks and the recommendations for future work, respectively.

CHAPTER 2

1-D MODELING AND SIMULATION OF FSI FOR BLAST WAVE MITIGATION

In this chapter, the dynamic response of a free-standing plate subjected to a blast wave is studied numerically to investigate the effects of fluid structure interactions (FSI) in blast wave mitigation. Previous work on the FSI between a blast wave and a free-standing plate (Kambouchev et al. [1]) has assumed a constant atmospheric pressure in the back of the plate and neglected the resistance caused by the shock wave formation due to the receding motion of the plate. This chapter develops a 1-D model, which includes the blast wave reflection from a free-standing plate, the plate motion and the resistance caused by the shock wave formation in the back of the plate. This 1-D model is validated by comparing results with numerical and analytical results available in the literature for special cases and good agreement is observed. The numerical results show that the effects of the interaction between the plate and the shock wave formation in the back of the plate should be considered in the blast wave mitigation.

2.1 Mathematical Formulation and Numerical Approach

2.1.1 Governing Equations

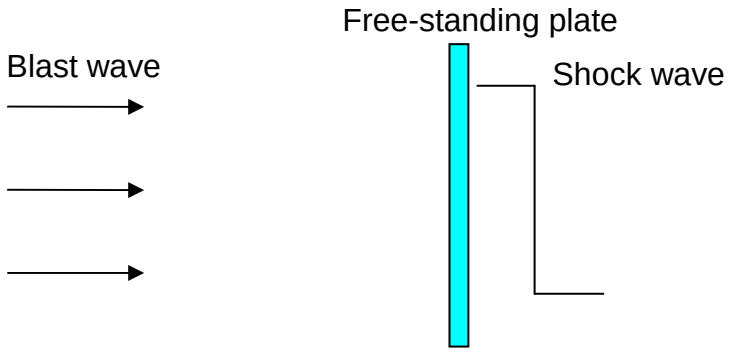

Figure 2.1: Schematic of a free-standing plate subjected to a blast wave

The schematic of the FSI between a blast wave and a free-standing plate is shown in Figure 2.1. The plate separates the computational domain into two parts: flow field in front of the plate and flow field in the back of the plate. The flow fields on both sides can be modeled as one-dimensional inviscid compressible flows, which are described by the Euler equations. They can be written in vector form as

$$\frac{\partial U}{\partial t}+\frac{\partial F}{\partial x}=0 \tag{2.1a}$$

where U is the solution vector, F is the flux vector, t is time and x is the space coordinate in the flow direction. U and F are given by

$$U=\begin{Bmatrix}\rho\\ \rho u\\ \rho e_t\end{Bmatrix} \qquad F=\begin{Bmatrix}\rho u\\ \rho u^2+p\\ (\rho e_t+p)u\end{Bmatrix} \tag{2.1b}$$

where ρ is density, p is pressure, u is velocity and e_t is the total energy per unit mass of the compressible flow. The total energy per unit mass is the sum of its internal energy per

unit mass, e, and its kinetic energy per unit mass, $u^2/2$. To close the governing equations, it is assumed that the compressible substance obeys the calorically perfect ideal gas law given by $p=\rho RT$ and $e=(RT)/(\gamma-1)$, where T is the temperature, R is the gas constant, and γ is the specific heat ratio. The specific heat ratio γ of 1.4 and the gas constant R for air of 287 J/(kg K) are used throughout this dissertation.

The free-standing plate is treated as a rigid body and the effects of deformation and stress-wave propagation within the plate are neglected. The free-standing plate obeys Newton's second law of motion

$$\frac{du_p}{dt} = \frac{\Delta p_p}{\rho_p h_p} \tag{2.2}$$

where u_p is the plate velocity, ρ_p is the plate density, h_p is the plate thickness, and Δp_p is the difference between the reflected pressure in front of the plate and the induced shock wave pressure in the back of the plate. The plate density ρ_p of 7800 kg/m^3 is used throughout this dissertation.

2.1.2 Initial and Boundary Conditions

The initial conditions for the flow fields (p_0, T_0, u_0) on both sides of the plate are prescribed as the ambient conditions, which are given by

$$p_0 = 101.3\,\text{kPa} \tag{2.3a}$$

$$T_0 = 298\,\text{K} \tag{2.3b}$$

$$u_0 = 0\,\text{m/s} \tag{2.3c}$$

The free-standing plate is initially at rest (u_p=0 m/s).

Two types of blast waves are studied in this chapter. The uniform blast wave can be written as

$$p(t) = p_u \tag{2.4}$$

where p_u is a constant overpressure of the blast wave. The second type simulates a typical exponential blast wave, which consists of an abrupt pressure increase followed by slow decay of pressure. There is usually a minor negative phase at the tail end of the blast wave. Neglecting the negative phase, the exponential blast wave can be approximated by an exponential profile

$$p(t) = p_{is} e^{-t/t_i} \tag{2.5}$$

where p_{is} is the peak overpressure of the initial blast wave which is at a stand-off distance d_i from the free-standing plate, and t_i is an initial decay time constant. The density and velocity of both types of blast waves are related to the overpressure through the classical Rankine-Hugoniot relations,

$$\rho(t) = \rho_0 \frac{(\gamma+1)p(t) + 2\gamma p_0}{(\gamma-1)p(t) + 2\gamma p_0} \tag{2.6a}$$

$$u(t) = \sqrt{\frac{2}{\gamma p_0}} \frac{a_0 p(t)}{\sqrt{(\gamma+1)p(t) + 2\gamma p_0}} \tag{2.6b}$$

The above Equations (2.4)-(2.6b) serve as the left-hand side boundary conditions for the flow field in front of the plate. The detailed derivation of Rankine-Hugoniot relations is presented in Appendix A. On the right-hand side of this flow field, zero gradient boundary conditions are applied to pressure and density. The no-penetration condition is applied to the velocity. These boundary conditions can be written as

$$\frac{\partial p}{\partial x} = 0 \tag{2.7a}$$

$$\frac{\partial \rho}{\partial x} = 0 \tag{2.7b}$$

$$u = u_p \tag{2.7c}$$

The computational domain for the flow field in front of the plate spans from the initial blast wave to the free-standing plate.

The left-hand side boundary conditions for the flow field in the back of the plate are the same as the right-hand side boundary conditions for the flow field in front of the plate. The right-hand side boundary conditions for the flow field in the back of the plate are given by the ambient conditions and can be written as

$$p = p_0 \tag{2.8a}$$

$$\rho = \rho_0 \tag{2.8b}$$

$$u = u_0 \tag{2.8c}$$

The computational domain for the flow field in the back of the plate should be large enough so that the right boundary conditions will not be affected by the induced shock wave.

2.1.3 Numerical Approach

The Euler equations for the flow fields in the front and in the back of the plate are solved using the Van Leer flux vector splitting scheme [54, 55] coupled with the monotone upstream-centered scheme for conservation laws (MUSCL) and Runge-Kutta scheme. Because there are sharp gradients in the flow fields for blast wave reflection and

shock wave generation, numerical dissipation is needed in the numerical scheme to attenuate numerical errors of small wavelengths. A standard upwind scheme can provide sufficient numerical dissipation for most flow problems which can involve shock waves with large gradients. However, the directions of characteristic velocity should be established before the upwind scheme can be implemented. The Van Leer flux vector splitting scheme is applied to split the flux vector F into forward and backward components F^+ and F^- in terms of the local Mach number. The Van Leer flux vector splitting scheme in 1-D coordinates is given by

$$F^+ = F, F^- = 0 \qquad for \qquad M \geq 1 \tag{2.9a}$$

$$F^+ = 0, F^- = F \qquad for \qquad M \leq -1 \tag{2.9b}$$

$$F^\pm = \left\{ \begin{array}{l} f_1^\pm \\ f_1^\pm \left[(\gamma - 1)u \pm 2a \right] / \gamma \\ f_1^\pm \left[(\gamma - 1)u \pm 2a \right]^2 / \left[2(\gamma^2 - 1) \right] \end{array} \right\} \qquad for \qquad -1 < M < 1 \tag{2.9c}$$

where

$$f_1^\pm = \pm \rho a \left[\frac{1}{2}(M \pm 1) \right]^2$$

After splitting, F^+ and F^- have characteristic velocities in forward and backward directions, respectively. MUSCL is then used to discretize the spatial derivative of the flux vector. MUSCL is a first order upwind scheme in the vicinity of the shock, and a second order upwind scheme elsewhere in the flow field. It provides good stability as well as accuracy. The approximation of $\partial F / \partial x$ is given by

$$\left(\frac{\partial F}{\partial x}\right)_i = \frac{1}{\Delta x}\left[F^+\left(U^-_{i+1/2}\right) - F^+\left(U^-_{i-1/2}\right) + F^-\left(U^+_{i+1/2}\right) - F^-\left(U^+_{i-1/2}\right)\right] \tag{2.10}$$

where the notation $F^{\pm}\left(U^{\mu}\right)$ denotes $F^{\pm}$ are evaluated at U^{μ}. U^{μ} are given by

$$U^-_{i+1/2} = U_i + \left\{s/4\left[(1-ks)\Delta_- + (1+ks)\Delta_+\right]\right\}_i \tag{2.11a}$$

$$U^+_{i+1/2} = U_{i+1} - \left\{s/4\left[(1-ks)\Delta_+ + (1+ks)\Delta_-\right]\right\}_{i+1} \tag{2.11b}$$

where

$$\left(\Delta_+\right)_i = U_{i+1} - U_i$$

$$\left(\Delta_-\right)_i = U_i - U_{i-1}$$

The spatial differencing is second order central difference scheme when $k = 1$. s is the limiter, which governs the accuracy of the approximation. The limiter is introduced to locate regions where the solution is discontinuous, such as shock waves, and is required to eliminate oscillations in those regions, and is given by

$$s = \frac{2\Delta_+\Delta_- + \varepsilon}{\left(\Delta_+\right)^2 + \left(\Delta_-\right)^2 + \varepsilon} \tag{2.12}$$

where ε is a small number ($\varepsilon = 10^{-6}$) preventing division by zero in regions of null gradients.

A second-order Runge-Kutta explicit scheme is used to discretize the temporal derivatives of the Euler equations, written as

$$U_i^* = U_i^n - \frac{1}{2}\Delta t\left(\frac{\partial F}{\partial x}\right)_i^n \tag{2.13a}$$

$$U_i^{n+1} = U_i^n - \Delta t\left(\frac{\partial F}{\partial x}\right)_i^* \tag{2.13b}$$

A second-order Runge-Kutta explicit scheme is used to discretize the Newton's

second law of motion for the free-standing plate, written as

$$u_p^* = u_p^n + \frac{\Delta t}{2}\left(\frac{\Delta p_p}{\rho_p h_p}\right)^n \tag{2.14a}$$

$$u_p^{n+1} = u_p^n + \Delta t\left(\frac{\Delta p_p}{\rho_p h_p}\right)^* \tag{2.14b}$$

Due to the receding motion of the free-standing plate, the domain in front of the plate and in the back of the plate varies during the FSI process. The displacement of the plate is obtained through

$$x_p^{n+1} = x_p^n + u_p^* \Delta t \tag{2.15}$$

Linear interpolation is used to update the solution vector *U* in the Euler equations for the different grid points and different time steps.

2.2 Numerical Validation

To verify the accuracy of the numerical model developed in this chapter, the flow fields in the front and in the back of the plate are simulated separately and compared with results available in the literature.

2.2.1 Model Validation: Part I

The simulation of the flow field in front of the free-standing plate, which is subjected to an exponential blast wave, is presented first. The resistance to the plate motion is neglected by assuming a constant atmospheric pressure in the back of the plate. The FSI problem under this assumption was investigated by Kambouchev et al. [1]. Based on the asymptotic limits for extremely light and extremely heavy plates placed within an air

environment, they developed a semi-analytical formula to predict the ratio of impulse transmitted to the plate (I_p) to the incident impulse (I_i)

$$\frac{I_p}{I_i} = \gamma_R \left(\frac{C_R f_R}{\gamma_R} \right)^{\beta_s/(1+\beta_s)} \beta_s^{\beta_s/(1-\beta_s)} \tag{2.16}$$

where

$$C_R = 2\frac{7 + 4p_s/p_0}{7 + p_s/p_0}$$

$$f_R = \left(6\frac{p_s}{p_0} + 7 \right) \times \sqrt{\frac{(6 + C_R)(p_s/p_0) + 7}{(p_s/p_0 + 7)[(1 + 6C_R)(p_s/p_0) + 7][C_R(p_s/p_0) + 7]}}$$

$$\gamma_R = \lim_{\rho_p h_p \to \infty} \frac{I_p}{I_i} = 8 - 42\frac{p_0}{p_s} \ln\left(1 + \frac{p_s}{7p_0} \right)$$

$$\beta_s = \frac{\rho_s U_s t_i}{\rho_p h_p}$$

Here p_s is the peak overpressure of incident blast wave, ρ_s is the density behind the incident shock front, U_s is the incident blast wave propagation speed, and β_s is a nondimensional parameter describing FSI and is inversely proportional to the plate thickness h_p. Kambouchev et al. [1] compared the ratio I_p/I_i obtained from the above formula with that obtained from their numerical model for different blast intensities and different plate thicknesses. It was observed that the approximate formula matches the numerical results not only in the light and heavy plate limits, but also in the intermediate range.

The numerical results in this chapter are compared with results from Kambouchev et al. [1] for two different blast intensities of 3.29 and 10.85, and at six different plate

thicknesses, as shown in Figure 2.2. It can be seen that the numerical results of the present study agree well with the previous results from Kambouchev et al. [1]. The ratio of impulse I_p/I_i decreases with increase of β_s (decrease of plate thickness). For thin plates (large β_s), the ratio of impulse I_p/I_i becomes very small for both blast intensities. This means that the blast wave mitigation using a thin plate is very effective. For thick plates (small β_s), the ratio of impulse remains fairly constant. For relatively thick plates, there is no significant blast wave mitigation.

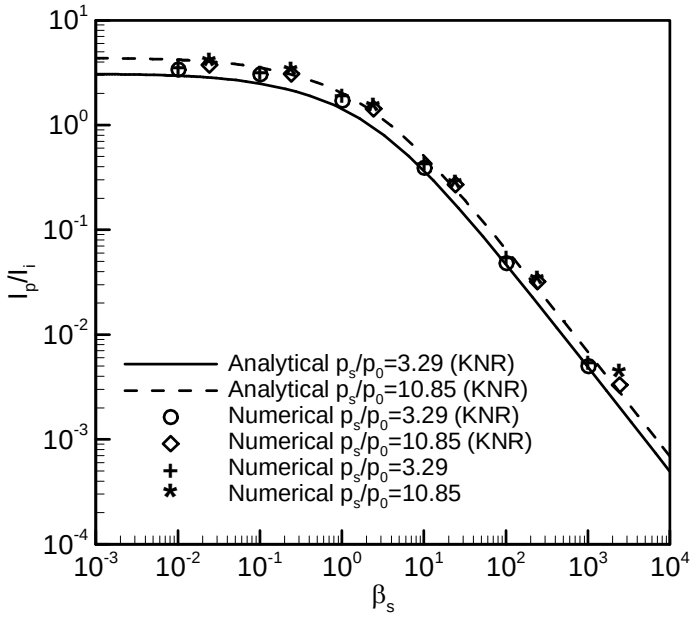

Figure 2.2: The ratio of impulse vs. compressible FSI parameter for different blast intensities

2.2.2 Model Validation: Part II

The flow field behind the plate is simulated by including the resistance to the plate motion. A shock wave is induced in the back of the plate due to the plate motion. When

the free-standing plate in the left boundary moves with a constant velocity u_p, the overpressure of the shock wave induced by the plate motion is available analytically [56]

$$u_p = a_0 \left(\frac{(2/\gamma)\dfrac{p_g}{p_0}}{2\gamma \dfrac{p_0}{p_g} + (\gamma + 1)} \right)^{1/2} \tag{2.17}$$

where p_g is overpressure in the back of the shock front, and u_p is the velocity of the plate. With a known value of u_p, the overpressure p_g can be determined using Equation (2.17).

A plate moving at constant velocity induces a shock wave, which propagates at a higher speed in the same direction as the plate motion. The pressure profiles of the induced shock wave obtained from the FSI model are compared with the analytical solutions at different times of 0.1 ms and 0.5 ms, and for plate velocities of 100 m/s and 10000 m/s. These two plate velocities are used to demonstrate the validity of the numerical model. It can be observed that the numerical results are in good agreement with the analytical solutions. The starting point of each curve at different times of 0.1 ms and 0.5 ms indicates the position of the free-standing plate. As shown in Figure 2.3, the shock wave strength induced by the plate velocity of 10000 m/s is many orders of magnitude larger than that induced by the plate velocity of 100 m/s.

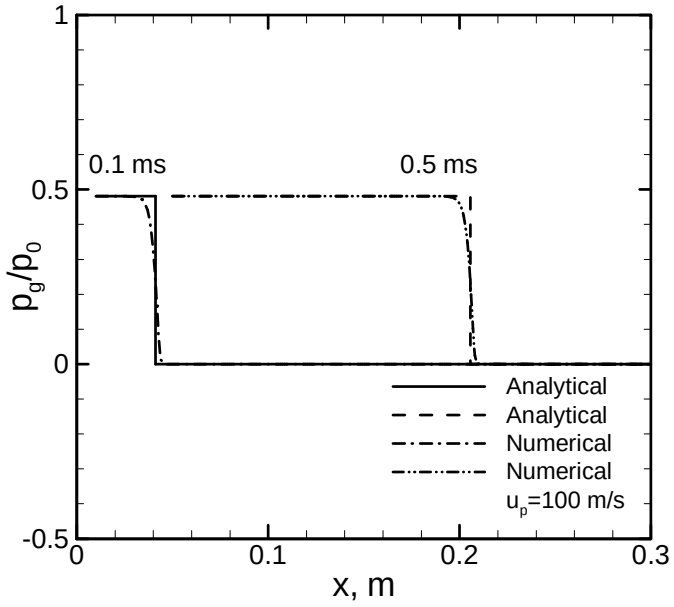

(a) low plate velocity

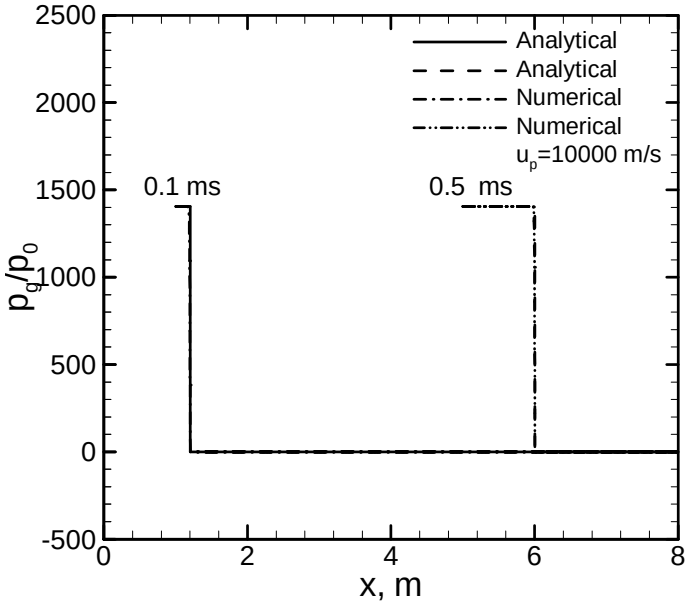

(b) high plate velocity

Figure 2.3: Numerical and analytical pressure profiles of the induced shock wave behind the plate for (a) low and (b) high plate velocities at different times

2.3 Results and Discussion

The numerical simulations of the FSI between a blast wave and a free-standing plate are carried out. The shock wave induced in the back of the plate is taken into account. In this model, the flow fields on both sides of the plate are coupled through the receding motion of the plate.

2.3.1 Uniform Blast Wave

As discussed before, the FSI between the receding plate and the induced shock wave in the back of the plate will affect the blast wave reflection. The reflection coefficient C is typically defined as the ratio of the reflected blast wave overpressure to the incident blast wave overpressure. The reflection coefficient is analyzed for a free-standing plate subjected to a uniform blast wave. There are two limiting cases of this physical problem. One corresponds to a plate of infinite mass and the other one corresponds to a plate of infinitesimal mass. For a free-standing plate of infinite mass, the reflection coefficient corresponds to that for a fixed wall, which has been derived previously and can be written as [5]

$$C = \frac{p_r}{p_s} = \frac{(3\gamma - 1)p_s / p_0 + 4\gamma}{(\gamma - 1)p_s / p_0 + 2\gamma} \tag{2.18}$$

where p_r is the reflected overpressure, and p_s is the incident overpressure. For air, the range of the reflection coefficient for a plate of infinite mass is

$2 \le C \le 8$.

The minimum value of 2 corresponds to an acoustic reflection, and the maximum value of 8 corresponds to a strong blast wave reflection.

For a free-standing plate of infinitesimal mass, the inertial effect of the plate is negligible. As the blast wave impacts the plate, the plate accelerates instantaneously to the equilibrium state. This implies that the force exerted by the reflected blast wave in front of the plate should be the same as that exerted by the induced shock wave in the back of the plate.

As discussed in section 2.2.2, the shock wave strength p_g/p_0 induced by the plate motion is related to the plate velocity u_p through Equation (2.17). The reflected blast wave strength is related to the plate velocity u_p through the Rankine-Hugoniot relations. It should be noted that the Rankine-Hugoniot relations for a reflected uniform blast wave are different from the Rankine Hugoniot relations for an incident uniform blast wave. They can be expressed as

$$\frac{W_r + u_s}{W_r + u_p} = \frac{(\gamma+1)\dfrac{p_r - p_s}{p_s + p_0} + 2\gamma}{(\gamma-1)\dfrac{p_r - p_s}{p_s + p_0} + 2\gamma} \tag{2.19}$$

where p_r is the reflected blast wave overpressure, p_s is the incident blast wave overpressure, and u_s is the fluid velocity behind the incident shock front, given by

$$u_s = a_0 \left(\frac{(2/\gamma)\dfrac{p_s}{p_0}}{2\gamma \dfrac{p_0}{p_s} + (\gamma+1)} \right)^{1/2} \tag{2.20}$$

W_r is the reflected blast wave speed, given by

$$W_r = a_r M_r - u_s \tag{2.21}$$

The Mach number of the reflected blast wave, M_r, is given by

$$M_r = \sqrt{\left(\frac{\gamma+1}{2\gamma}\right)\left(\frac{p_r - p_s}{p_s + p_0}\right)+1} \tag{2.22}$$

The speed of sound a_r is related to T_s, the temperature behind the incident shock front, through the equation

$$a_r = \sqrt{\gamma R T_s} \tag{2.23}$$

T_s is given by

$$T_s = T_0\left[\left(\frac{\gamma-1}{2\gamma}\right)\frac{p_s}{p_0}+1\right]\left(\frac{\frac{p_s}{p_0}+1}{\left(\frac{\gamma+1}{2\gamma}\right)\frac{p_s}{p_0}+1}\right) \tag{2.24}$$

For a free-standing plate of infinitesimal mass, p_g equals to p_r. Combining Equations (2.19)-(2.24) and Equation (2.17) yields a reflection coefficient p_r/p_s of 1. The detailed derivation of Equations (2.19) to (2.24) is presented in Appendix A.

Numerical simulations of the FSI are carried out for 4 different plate thicknesses: infinite thickness (fixed wall), 50 mm, 15 mm, and 5 mm. In Figure 2.4, the numerical results for a fixed wall and for a plate of infinitesimal mass are compared with the analytical solutions that correspond to these limiting cases. It can be seen that the numerical results for an infinite plate thickness agree well with the analytical results for a fixed wall. The reflection coefficient increases from 2 to 8 with the increase of incident blast intensity. For small incident blast intensity, all free-standing plates are relatively

heavy to the incident blast wave. Therefore, the reflection coefficient for all free-standing plates approaches asymptotically that of a fixed wall. Figure 2.4 also shows that, as the incident blast intensity increases, the reflection coefficient deviates from that of the fixed wall gradually due to the FSI. The inception of the deviation for a thin plate starts earlier than that for a thick plate. There is a critical transition point for a particular plate thickness. When the incident blast intensity is greater than the critical transition value, the reflection coefficient starts to decrease. It indicates that the FSI plays a more important role for large blast intensities. As the blast intensity increases further, the reflection coefficient of the free-standing plate of finite mass gradually approach to that of a plate of infinitesimal mass. As shown in Figure 2.4(a), the reflection coefficient for the 5 mm thick plate approaches 1 asymptotically when the blast intensity exceeds 30. The reflection coefficient for plates of 15 mm and 50 mm approaches 1 as the blast intensity continues to increase (see Figure 2.4(b)). It should be noted that the reflection coefficient can never be less than 1. Since the transmitted impulse is related to the reflected pressure, the ratio of transmitted impulse to the incident impulse I_p/I_i is always larger than 1. In a previous model [1], it was predicted that I_p/I_i approaches 0 for relatively light plates by neglecting the resistance in the back of the plate. The previous model over-predicts the effectiveness of FSI in blast wave mitigation.

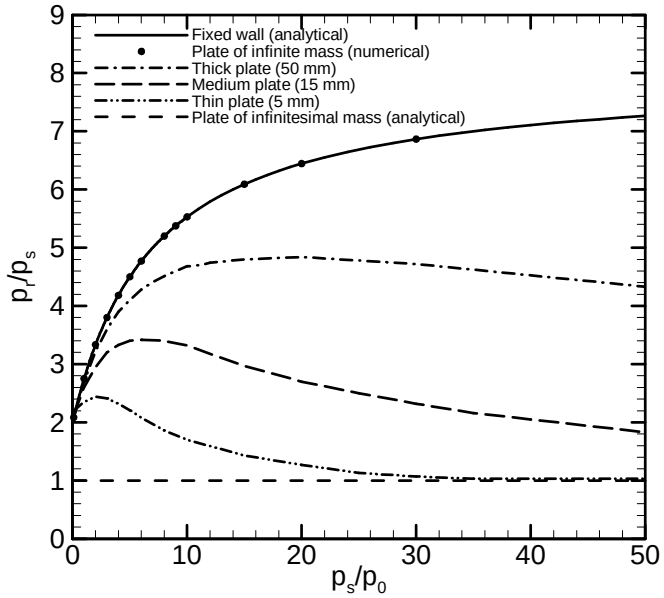

(a)

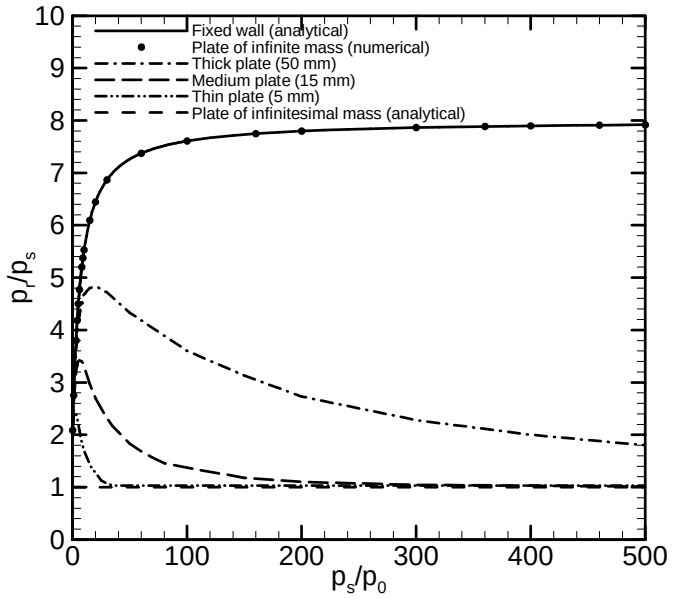

(b)

Figure 2.4: The reflection coefficient for different plate thicknesses at different uniform incident blast intensities. (a) Uniform incident blast intensities of 0-50; (b) Uniform incident blast intensities of 0-500

2.3.2 Exponential Blast Wave

Simulations of an exponential blast wave interacting with a free-standing plate are conducted for different blast intensities and plate thicknesses. Because both the incident pressure and reflected pressure vary with time for the exponential blast wave, the reflection coefficient as defined in the previous section can not be applied to the exponential blast wave. Therefore, the reflected overpressure p_r and the incident overpressure p_s are integrated over the duration of the blast wave. The ratio of the impulse transmitted to the plate I_p and the incident impulse I_i, is equivalent to the reflection coefficient for uniform blast wave.

A blast wave with a peak overpressure of 2 MPa, decay time constant of 0.5 ms, and stand-off distance of 1.6 m is adopted for the numerical simulation. This results in a peak blast intensity of 10.85 right in front of the plate. Approximately the same plate thicknesses (0.000378, 0.00378, 0.0378, 0.378, 3.78, and 37.8 mm) as in Reference 1 have been simulated. The ratio of impulse transmitted to the plate (I_p) to the incident impulse (I_i) for low blast intensity of 10.85, with resistance in the back of the plate, is shown in Figure 2.5. For relatively heavy plates, the impact of incident blast wave results in a relatively small receding velocity. This implies that the blast wave mitigation effects of FSI for relatively heavy plates are insignificant. As the thickness of the plate decreases, the receding velocity of the plate increases. The ratio of impulse I_p/I_i decreases. For thicknesses less than about 0.378 mm, the ratio of impulse I_p/I_i reaches a plateau. This is due to the increased resistance in the back of the plate. The impact of the

blast wave drives the relatively light plate to very high receding velocity, which induces a strong shock wave in the back of the plate. When the shock wave strength in the back of the plate becomes comparable to the incident blast intensity, the effectiveness of FSI in reducing the blast wave impulse diminishes.

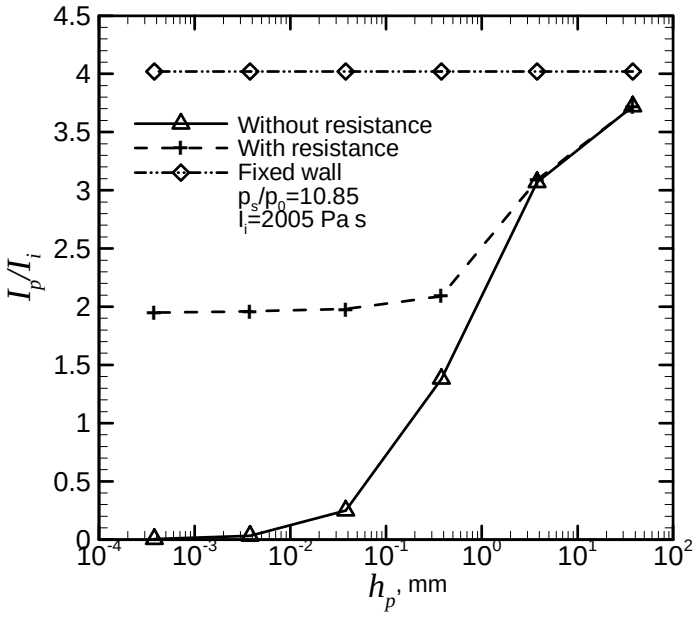

Figure 2.5: Comparison between the ratio of impulse I_p/I_i with and without resistance for low blast intensity at different plate thicknesses

The FSI between a blast wave and a free-standing plate without considering shock wave formation in the back of the plate [1] is also shown in Figure 2.5. For relatively heavy plates, the effects of resistance on FSI are not very important. The difference between the ratio of impulse I_p/I_i with and without resistance is very small. As the thickness of the plate decreases, the effects of resistance increase. The difference between the ratio of impulse I_p/I_i with and without resistance becomes significant. While the

previous model [1] predicts that it is possible to achieve 100% reduction with a light free-standing plate by neglecting the resistance in the back of the plate, the ratio of impulse I_p/I_i is limited by the resistance in the back of the plate to around 2 for a blast intensity of 10.85. This agrees with the results obtained in previous section. As expected, the ratio of transmitted impulse to the incident impulse I_p/I_i is always larger than 1. Hence, the previous model significantly over-predicts the effectiveness of FSI in reducing the blast wave impact. For this low blast intensity, the range of small plate thicknesses where the two physical models differ in blast wave mitigation is of limited practical value. However, the difference becomes important for more realistic conditions presented in Figure 2.6 and Figure 2.7.

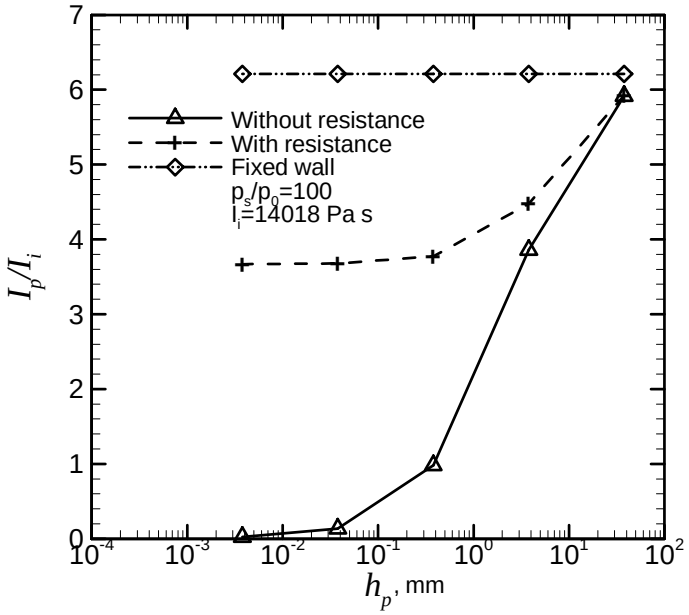

Figure 2.6: Comparison between the ratio of impulse I_p/I_i with and without resistance for higher blast intensity at different plate thicknesses

Results for a blast intensity of 100 are presented in Figure 2.6. A blast wave with a peak overpressure of 16 MPa, decay time constant of 0.5 ms, and stand-off distance of 3.2 m is adopted. These parameters result in a peak blast intensity of 100 right in front of the plate. Five different plate thicknesses ranging from 0.00378 to 37.8 mm are simulated. The FSI between a blast wave and a free-standing plate for a blast intensity of 100 behaves very much similar to the blast intensity of 10.85. It was found that the ratio of impulse I_p/I_i reaches a limit of 3.6 for thin plates. The effectiveness of FSI in blast wave mitigation decreases with the increased blast intensity.

Additional simulations are conducted with a blast intensity of 1000. This is achieved by placing a blast wave with a peak overpressure of 150 MPa, decay time constant of 0.5 ms at a stand-off distance of 9.6 m. Four different plate thicknesses ranging from 0.0378 to 37.8 mm are simulated. For this blast wave, the ratio of impulse I_p/I_i reaches a limit of 5.4 for thin plates. The difference between the ratio of impulse I_p/I_i with and without resistance becomes 100% for plate thickness of 3.78 mm. As the blast intensity reaches 1000, the relatively thick plate of 3.78 mm is relatively light for the blast wave. Therefore, the resistance in the back of the plate significantly affects the FSI. Neglecting the resistance causes large error in predicting the ratio of impulse I_p/I_i.

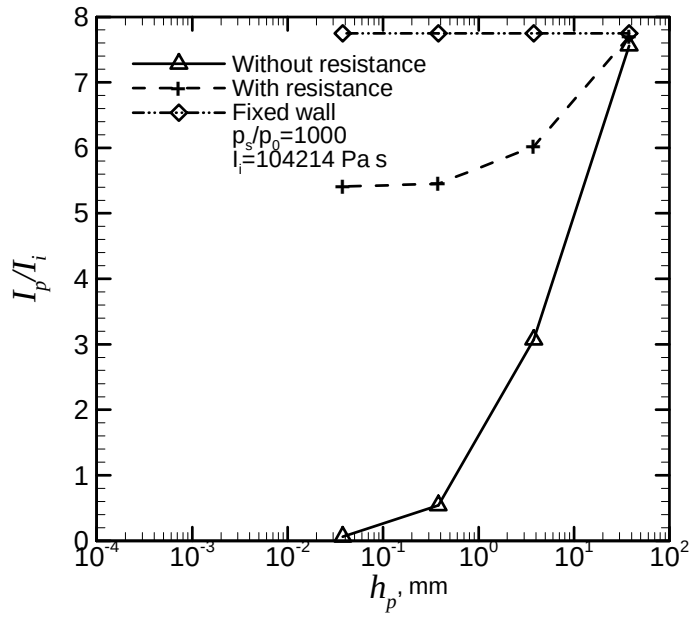

Figure 2.7: Comparison between the ratio of impulse I_p/I_i with and without resistance for typical blast wave at different plate thicknesses

The ratio of impulse I_p/I_i is not only affected by the incident peak blast intensity, but also by the incident impulse. For a particular incident peak blast intensity, different decay time constants generate different incident impulses. Simulations of a blast wave interacting with a free-standing plate of 3.78 mm are conducted for different incident blast impulses. A blast wave with an initial peak overpressure of 8 MPa, decay time constants ranging from 0.1 to 1.0 ms are placed at different stand-off distances to obtain a constant peak blast intensity of 50 and decay time constants ranging from 0.14 to 1.9 ms right in front of the plate with different incident impulses. For an infinitesimal impulse, the pressure instantaneously decays to below the ambient pressure. Therefore, the impulse is completely transmitted to the free-standing plate before it recedes and the FSI

has no effect in reducing the blast wave impulse. Hence, the ratio of transmitted impulse to the incident impulse I_p/I_i for an infinitesimal impulse is the same as that on a fixed wall. For a uniform blast wave with incident blast intensity of 50, the ratio of impulse on a fixed wall is 7.28. The reflection coefficient is identical to the ratio of impulse for a uniform blast wave. Since the reflection coefficient for a fixed wall decreases with the decrease of blast intensity, it can be expected that the ratio of impulse of an exponential blast wave will be less than that of a uniform blast wave. It can be seen from Figure 2.8 that the ratio of impulse for an exponential blast wave with infinitesimal impulse is slightly below 7.28. As the incident impulse increases, the free-standing plate will recede at a higher velocity. The FSI between the blast wave and the free-standing plate results in the decrease of transmitted impulse as well as the ratio of impulse.

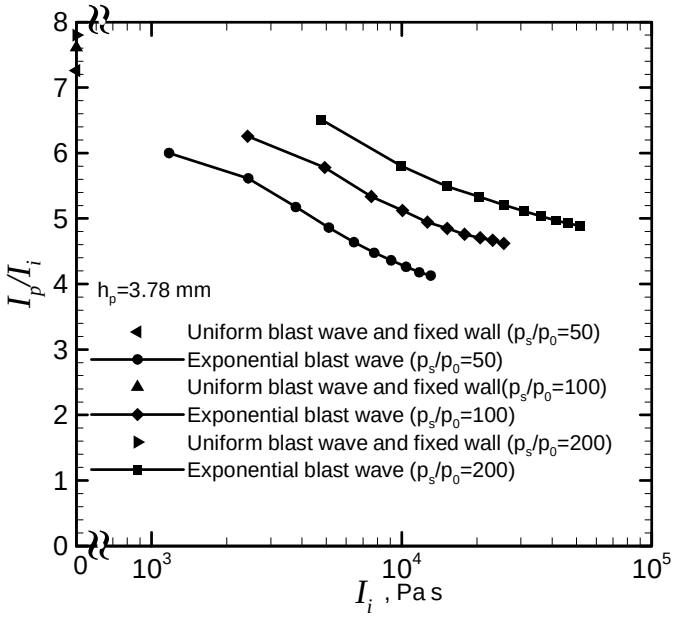

Figure 2.8: The ratio of impulse I_p/I_i as a function of incident impulse I_i

For initial peak overpressures of 16 MPa and 32 MPa and decay time constants ranging from 0.1 to 1.0 ms, different stand-off distances are used to obtain peak blast intensities of 100 and 200 right in front of the free-standing plate, where decay time constants ranges from 0.15 to 2.0 ms. The ratio of impulse for peak blast intensities of 100, and 200 behaves the same as that for peak blast intensities of 50. It can be seen from Figure 2.8 that increased peak blast intensity results in an increase of ratio of impulse.

2.4 Conclusions

A numerical model of the FSI between a blast wave and a free-standing plate has been developed. Both the blast wave reflection in front of the plate and the shock wave induced in the back of the plate are considered in the model. The numerical model is validated by comparing it with analytical and numerical results of simple cases. Two types of blast wave, uniform and exponential blast wave, are investigated in this chapter. For a uniform blast wave, the FSI of a heavy plate resembles the blast wave reflection off a fixed wall. It was shown that the blast wave reflection of a free-standing plate of infinitesimal mass results in an acoustic reflection of a blast wave. The impact on the plate is identical to the incident blast wave pressure. The FSI of a free-standing plate with finite mass falls between these two limiting cases. As the blast intensity increases, the reflection coefficient of the free-standing plate asymptotically approaches 1.

For an exponential blast wave, numerical results show that the effectiveness of FSI in blast wave mitigation increases as the thickness of the plate decreases. However, the

effectiveness reaches a plateau after the thickness decreases beyond a critical value. This is due to the increased resistance in the back of the plate. As the thickness of the plate decreases, the impact of the blast wave drives the plate to ever higher receding velocity, which induces a stronger shock wave in the back of the plate. When the shock wave strength in the back of the plate becomes comparable to the blast intensity, the effectiveness of FSI in reducing the blast wave impulse diminishes. The model shows that the resistance in the back of the plate plays an important role in the FSI, especially for relatively light plates. Neglecting the resistance in the previous model significantly over-predict the effectiveness of FSI. Numerical investigation of the FSI between a blast wave and a free-standing plate also reveals that the ratio of impulse is also highly dependent on the incident blast intensity and impulse. For a particular incident blast intensity, a small decrease in the incident impulse can significantly increase the ratio of impulse. For a constant incident impulse, the increased blast intensity results in an increase of ratio of impulse.

CHAPTER 3

2-D MODELING AND SIMULATION OF INTERACTIONS BETWEEN BLAST WAVES AND V-SHAPED AND CONE-SHAPED STRUCTURES

In this chapter, a 2-D numerical model of interactions between a blast wave and a V-shaped or a cone-shaped structure is developed. The model simulates the blast wave reflection from a V-shaped or a cone-shaped structure, the movement of the structure and the induced shock wave behind the structure. The solution of flow fields is accomplished by solving transformed Euler equations in rectangular computational domain. The model is validated by comparing results with analytical solutions available in the literature for special cases and good agreement is achieved. Different types of blast wave reflections, such as normal reflection, oblique reflection and Mach stem reflection, are captured by the numerical model. The numerical results show that the FSI coupled with oblique or Mach stem reflection improves the blast wave mitigation.

3.1 Mathematical Formulation and Numerical Approach

The schematic of interactions between a blast wave and a V-shaped or a cone-shaped structure is shown in Figure 3.1. Due to symmetry, it is sufficient to simulate only one half of the flow field, which is shown by the dashed lines in Figure 3.1.

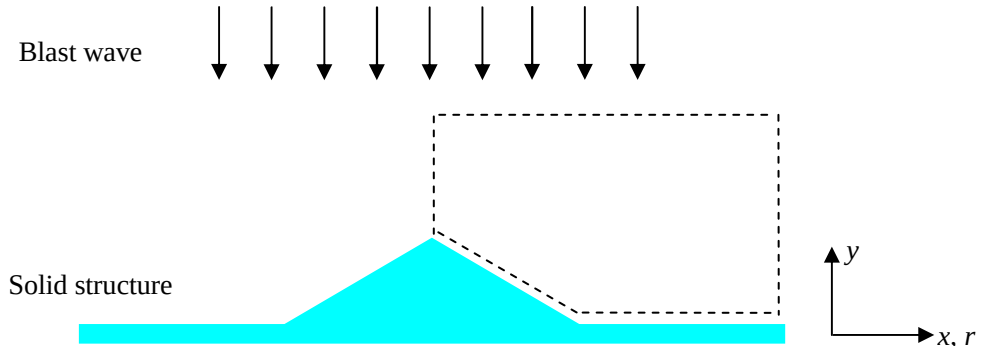

Figure 3.1: Schematic of a V-shaped or a cone-shaped structure subjected to a blast wave

3.1.1 Governing Equations

3.1.1.1 For a V-Shaped Structure Subjected to a Blast Wave

The flow field for a V-shaped structure subjected to a blast wave can be described by the 2-D Euler equations in Cartesian coordinates and written in vector form as [57]

$$\frac{\partial U}{\partial t}+\frac{\partial F}{\partial x}+\frac{\partial G}{\partial y}=0 \tag{3.1a}$$

where U is the solution vector, F and G are the flux vectors, t is time and x and y are the space coordinates in the 2-D Cartesian coordinates. U, F, and G are given by

$$U=\begin{Bmatrix}\rho\\ \rho u_x\\ \rho u_y\\ \rho e_t\end{Bmatrix} \quad F=\begin{Bmatrix}\rho u_x\\ \rho u_x^2+p\\ \rho u_x u_y\\ (\rho e_t+p)u_x\end{Bmatrix} \quad G=\begin{Bmatrix}\rho u_y\\ \rho u_x u_y\\ \rho u_y^2+p\\ (\rho e_t+p)u_y\end{Bmatrix} \tag{3.1b}$$

where ρ is density, p is pressure, u_x and u_y are the velocity components in x and y direction respectively and e_t is the total energy per unit mass of the compressible flow. The total energy per unit mass is the sum of its internal energy per unit mass, e, and its kinetic energy per unit mass, $(u_x^2+u_y^2)/2$. The compressible substance is assumed to obey

the calorically perfect ideal gas law, given by $p=\rho RT$ and $e=(RT)/(\gamma-1)$, where T is the temperature, R is the gas constant, and γ is the specific heat ratio. The specific heat ratio γ of 1.4 and the gas constant R for air of 287 J/(kg K) are used throughout this dissertation.

3.1.1.2 For a Cone-Shaped Structure Subjected to a Blast Wave

For a blast wave impacting a cone-shaped structure, the flow field can be described by the 2-D Euler equations in cylindrical coordinates and written in vector form as [57]

$$\frac{\partial U}{\partial t}+\frac{\partial F}{\partial r}+\frac{\partial G}{\partial y}=S \tag{3.2a}$$

where S is the source vector and r and y are the space coordinates in the 2-D cylindrical coordinates. U, F, G and S are given by

$$U=r\begin{Bmatrix}\rho\\ \rho u_r\\ \rho u_y\\ \rho e_t\end{Bmatrix}\quad F=r\begin{Bmatrix}\rho u_r\\ \rho u_r^2+p\\ \rho u_r u_y\\ (\rho e_t+p)u_r\end{Bmatrix}\quad G=r\begin{Bmatrix}\rho u_y\\ \rho u_r u_y\\ \rho u_y^2+p\\ (\rho e_t+p)u_y\end{Bmatrix}\quad S=\begin{Bmatrix}0\\ p\\ 0\\ 0\end{Bmatrix} \tag{3.2b}$$

Because of the similarity between the 2-D Euler equations in Cartesian coordinates and cylindrical coordinates, the model simulating a blast wave impacting a V-shaped structure can be easily modified to study a blast wave impacting a cone-shaped structure.

3.1.1.3 For a Free-Standing Structure

The free-standing structure is treated as a rigid body and the effects of deformation and stress-wave propagation within the structure are neglected. The structure obeys Newton's second law of motion

$$\frac{du_p}{dt} = \frac{\Delta F_p}{W_p} \tag{3.3}$$

where u_p is the velocity of structure, W_p is the mass of structure, and ΔF_p is the difference between the force in front of and behind the structure.

3.1.1.4 For the Flow Field behind the Structure

The flow field in the back of the structure can be described by the 1-D Euler equations in Cartesian coordinates and written in vector form as

$$\frac{\partial U}{\partial t} + \frac{\partial F}{\partial x} = 0 \tag{3.4a}$$

where U and F are given by

$$U = \begin{Bmatrix} \rho \\ \rho u \\ \rho e_t \end{Bmatrix} \qquad F = \begin{Bmatrix} \rho u \\ \rho u^2 + p \\ (\rho e_t + p)u \end{Bmatrix} \tag{3.4b}$$

3.1.2 Initial and Boundary Conditions

The initial conditions for the flow fields (p_0, T_0, u_0) are prescribed as the ambient conditions, which are given by

$$p_0 = 101.3\,\text{kPa} \tag{3.5a}$$

$$T_0 = 298\,\text{K} \tag{3.5b}$$

$$u_{x0} = 0\,\text{m/s} \tag{3.5c}$$

$$u_{y0} = 0\,\text{m/s} \tag{3.5d}$$

The free-standing structure is initially at rest (u_p=0 m/s).

Two types of blast waves are applied in this chapter: uniform and exponential. The uniform blast wave can be written as

$$p(t) = p_u \tag{3.6}$$

where p_u is a constant overpressure of the blast wave. The typical exponential blast wave can be approximated by an exponential profile [1]

$$p(t) = p_{is} e^{-t/t_i} \tag{3.7}$$

where p_{is} is the peak overpressure of the initial blast wave which is at a stand-off distance from a structure, and t_i is an initial decay time constant.

The density and velocity component in the y direction are related to the overpressure through the classical Rankine-Hugoniot relations. The velocity component in the x direction is 0 m/s.

$$\rho(t) = \rho_0 \frac{(\gamma+1)p(t) + 2\gamma p_0}{(\gamma-1)p(t) + 2\gamma p_0} \tag{3.8a}$$

$$u_y(t) = \sqrt{\frac{2}{\gamma p_0}} \frac{a_0 p(t)}{\sqrt{(\gamma+1)p(t) + 2\gamma p_0}} \tag{3.8b}$$

$$u_x(t) = 0 \tag{3.8c}$$

The above Equations (3.6)-(3.8c) serve as the inflow boundary conditions at $y=y_0$, where y_0 is a stand-off distance from the structure.

The outflow boundary conditions are applied along the right boundary at $x=x_0$, which can be written as

$$\left.\frac{\partial^2 (p, T, u_y, u_x)}{\partial x^2}\right|_{x=x_0} = 0 \tag{3.9}$$

where x_0 is physical domain in x direction.

The symmetric boundary conditions are applied along the centerline of a V-shaped or

a cone-shaped structure at x=0, which can be written as

$$\left.\frac{\partial\left(p,T,u_y\right)}{\partial x}\right|_{x=0}=0 \tag{3.10a}$$

$$u_x\big|_{x=0}=0 \tag{3.10b}$$

At the reflecting surface of a V-shaped or a cone-shaped structure, the flow must be tangent to the surface for an inviscid fluid. We force the normal-direction gradients of the pressure and temperature to be zero. The same boundary conditions in front of and behind the structure used in previous work [58] are applied. The boundary conditions in front of the reflecting surface of a V-shaped or a cone-shaped structure can be written as

$$\frac{\partial\left(p,T,u_x\right)}{\partial\vec{n}}=0 \tag{3.11a}$$

$$u_y=u_x\tan\beta+u_p \tag{3.11b}$$

where $\vec{n}$ is the surface normal, and β is the incident angle between the incident shock front and the reflecting surface, which is equal to the angle between the reflecting surface and the bottom of the structure.

The boundary conditions behind the reflecting surface of a V-shaped or a cone-shaped structure can be written as

$$\frac{\partial\left(p,T,u_x\right)}{\partial y}=0 \tag{3.12a}$$

$$u_y=u_p \tag{3.12b}$$

The far field boundary conditions for the flow field in the back of the structure are given by the ambient conditions and can be written as

$$p = p_0 \tag{3.13a}$$

$$\rho = \rho_0 \tag{3.13b}$$

$$u = u_0 \tag{3.13c}$$

The computational domain for the flow field in the back of the structure should be large enough so that the far field boundary conditions will not be affected by the induced shock wave.

3.1.3 Grid Generation and Coordinate Transformation

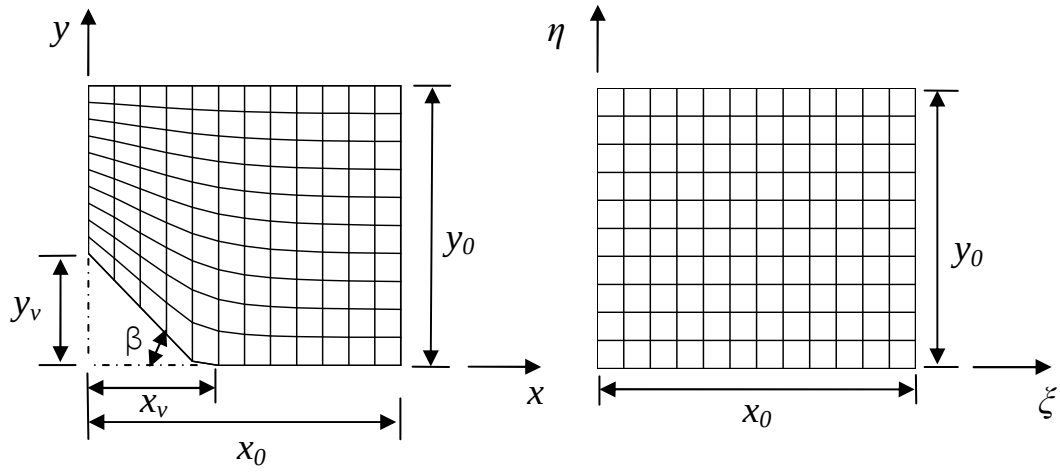

(a) (b)

Figure 3.2: Schematic of an elliptic grid generation. (a) physical domain; (b) computational domain

Since it is difficult to develop finite difference equations in the physical domain being studied, it is necessary to employ a general mapping to transform the irregular physical domain into a rectangular computational domain. Since this physical domain has well-defined geometric boundaries, an elliptic grid generator is used. The mapping is a

one-to-one correspondence between the rectangular grid in the computational domain, as shown in Figure 3.2(b), and the curvilinear grid in the physical domain, as shown in Figure 3.2(a). Complex boundaries are easily treated with the elliptic grid generator. The resulting grid from the elliptic grid generator is smooth. The mapping is constructed by specifying the desired grid points (x, y) on the boundary of the physical domain with the interior point distribution determined through the solution of the simplest elliptic equations, Laplace's equations, which are written as [59]

$$\xi_{xx} + \xi_{yy} = 0 \tag{3.14a}$$

$$\eta_{xx} + \eta_{yy} = 0 \tag{3.14b}$$

where (ξ, η) represent the coordinates in the computational domain. In the above Equations (3.14a) and (3.14b), ξ and η are dependent variables, while x and y are independent variables. The uniform grid in the computational domain is prescribed. In order to solve the (x, y) location of interior grid points in the physical domain, the above Equations (3.14a) and (3.14b) are transformed to the computational domain by interchanging the roles of the independent and dependent variables. This yields

$$\alpha x_{\xi\xi} - 2\beta x_{\xi\eta} + \gamma x_{\eta\eta} = 0 \tag{3.15a}$$

$$\alpha y_{\xi\xi} - 2\beta y_{\xi\eta} + \gamma y_{\eta\eta} = 0 \tag{3.15b}$$

where

$$\alpha = x_\eta^2 + y_\eta^2$$
$$\beta = x_\xi x_\eta + y_\xi y_\eta$$
$$\gamma = x_\xi^2 + y_\xi^2$$

The (x, y) location of interior grid points in the physical domain as a function of the (ξ, η) location of the corresponding grid points in the computational domain can be calculated through the transformed Equations (3.15a) and (3.15b). The detailed derivation of Equations (3.15a) and (3.15b) is presented in Appendix B.2.

When the governing equations are solved in the computational domain, they must be expressed in terms of the variables ξ and η. Therefore, the 2-D Euler equations are transformed from (x, y) to (ξ, η) as the new independent variables. The transformed Euler equations in Cartesian coordinates can be written in the conservation form as [57]

$$\frac{\partial \hat{U}}{\partial t} + \frac{\partial \hat{F}}{\partial \xi} + \frac{\partial \hat{G}}{\partial \eta} = 0 \tag{3.16}$$

where

$$\hat{U} = JU$$
$$\hat{F} = J\left(F\xi_x + G\xi_y\right)$$
$$\hat{G} = J\left(F\eta_x + G\eta_y\right)$$

Here Jacobian J in the above equations is given by

$$J = \frac{\partial(x, y)}{\partial(\xi, \eta)} \tag{3.17}$$

The transformed Euler equations in cylindrical coordinates are similar, which are given by

$$\frac{\partial \hat{U}}{\partial t}+\frac{\partial \hat{F}}{\partial \xi}+\frac{\partial \hat{G}}{\partial \eta}=\hat{S} \tag{3.18}$$

where

$\hat{S} = JS$

The detailed derivation of Equation (3.18) is presented in Appendix B.3.

The metrics in the above Equation (3.16), such as ξ_x, η_y, are obtained from finite differences. Since the grid in the irregular physical domain is non-uniform, the spaces between grid points, Δx and Δy, are not constants. However, the spaces between grid points in the rectangular computational domain, $\Delta\xi$ and $\Delta\eta$, are uniform. Therefore, the following equations [60] are adopted to obtain the metrics ξ_x, ξ_y, η_x, and η_y, given by

$$\xi_x = \frac{1}{J} y_\eta \tag{3.19a}$$

$$\eta_x = -\frac{1}{J} y_\xi \tag{3.19b}$$

$$\xi_y = -\frac{1}{J} x_\eta \tag{3.19c}$$

$$\eta_y = \frac{1}{J} x_\xi \tag{3.19d}$$

Central differences are used for the finite differences. For example,

$$x_\xi = \frac{x_{i+1,j} - x_{i-1,j}}{2\Delta\xi} \tag{3.20}$$

The detailed derivation of Equations (3.19a) to (3.19d) is presented in Appendix B.1.

3.1.4 Numerical Approach

The transformed Euler equations for the flow field in front of a V-shaped or a cone-shaped structure are solved using the Van Leer flux vector splitting scheme coupled with the monotone upstream-centered scheme for conservation laws (MUSCL) and

Runge-Kutta scheme. The Van Leer flux vector splitting scheme in 2-D Cartesian coordinates is given by [57]

$$\hat{F}^{+}=\hat{F},\qquad \hat{F}^{-}=0\qquad for\qquad M_{\xi}\geq 1 \tag{3.21a}$$

$$\hat{F}^{+}=0,\qquad \hat{F}^{-}=\hat{F}\qquad for\qquad M_{\xi}\leq -1 \tag{3.21b}$$

$$\hat{F}^{\pm}=J\sqrt{\xi_x^2+\xi_y^2}\begin{Bmatrix} e_1^{\pm} \\ e_1^{\pm}\left[\dfrac{\xi_x}{\gamma\sqrt{\xi_x^2+\xi_y^2}}\left(-\bar{u}_x\pm 2a\right)+u_x\right] \\ e_1^{\pm}\left[\dfrac{\xi_y}{\gamma\sqrt{\xi_x^2+\xi_y^2}}\left(-\bar{u}_x\pm 2a\right)+u_y\right] \\ e_1^{\pm}\left[\dfrac{-(\gamma-1)\bar{u}_x{}^2\pm 2(\gamma-1)a\bar{u}_x+2a^2}{(\gamma^2-1)}+\dfrac{u_x^2+u_y^2}{2}\right] \end{Bmatrix} for\quad -1<M_{\xi}<1 \tag{3.21c}$$

where

$$M_{\xi}=\frac{\xi_x u_x+\xi_y u_y}{a\sqrt{\xi_x^2+\xi_y^2}}$$

$$e_1^{\pm}=\pm\frac{1}{4}\rho a\left(M_{\xi}\pm 1\right)^2$$

$$\bar{u}_x=\frac{\xi_x u_x+\xi_y u_y}{\sqrt{\xi_x^2+\xi_y^2}}$$

$\hat{G}^{\pm}$ follows the same form as $\hat{F}^{\pm}$, where all the ξ are replaced by η. The Van Leer flux vector splitting scheme in 2-D cylindrical coordinates is similar to that in 2-D Cartesian coordinates, where the item $J\sqrt{\xi_x^2+\xi_y^2}$ in Equation (3.21c) is replaced by $Jr\sqrt{\xi_r^2+\xi_y^2}$.

After splitting flux vector, $\hat{F}^{+}$ and $\hat{F}^{-}$ have characteristic velocities in forward and backward directions, respectively. MUSCL is then used to discretize the spatial

derivatives of the flux vector. The approximation of $\partial\hat{F}/\partial\xi$ is given by

$$\left(\frac{\partial\hat{F}}{\partial\xi}\right)_i = \frac{1}{\Delta\xi}\left[\hat{F}^+\left(\hat{U}^-_{i+1/2}\right) - \hat{F}^+\left(\hat{U}^-_{i-1/2}\right) + \hat{F}^-\left(\hat{U}^+_{i+1/2}\right) - \hat{F}^-\left(\hat{U}^+_{i-1/2}\right)\right] \tag{3.22}$$

Replacing ξ with η in the above Equation (3.22) yields the calculation of $\partial\hat{G}/\partial\eta$. The evaluation of $\hat{U}^{\pm}_{i\pm1/2}$ is similar to the Equations (2.11a) and (2.11b) given in chapter 2, where *U* is replaced by $\hat{U}$. A second-order Runge-Kutta explicit scheme is used to discretize the temporal derivatives of the transformed Euler equations, written as

$$\hat{U}_i^* = \hat{U}_i^n - \frac{1}{2}\Delta t\left(\frac{\partial\hat{F}}{\partial\xi} + \frac{\partial\hat{G}}{\partial\eta} - \hat{S}\right)_i^n \tag{3.23a}$$

$$\hat{U}_i^{n+1} = \hat{U}_i^n - \Delta t\left(\frac{\partial\hat{F}}{\partial\xi} + \frac{\partial\hat{G}}{\partial\eta} - \hat{S}\right)_i^* \tag{3.23b}$$

For the 2-D transformed Euler equations in Cartesian coordinates, the source vector $\hat{S}$ is 0.

For a free-standing structure, a second-order Runge-Kutta explicit scheme is used to discretize the Newton's second law of motion for the free-standing structure, written as

$$u_p^* = u_p^n + \frac{\Delta t}{2}\left(\frac{\Delta F_p}{W_p}\right)^n \tag{3.24a}$$

$$u_p^{n+1} = u_p^n + \Delta t\left(\frac{\Delta F_p}{W_p}\right)^* \tag{3.24b}$$

Due to the receding motion of the free-standing structure, the physical domain in front of the structure and in the back of the structure varies during the interaction process. The displacement of the structure is obtained through

$$y_p^{n+1} = y_p^n + u_p^*\Delta t \tag{3.25}$$

Linear interpolation is used to update the solution vector $\hat{U}$ in the transformed Euler equations for the different grid points and different time steps.

When the solution vector $\hat{U}$ in the transformed Euler equations is obtained, the appropriate solution vector U in the Euler equations can be determined by applying the Jacobian of transformation J, with

$$U = J^{-1}\hat{U} \tag{3.26}$$

The numerical approach for the flow field in the back of the structure has been used in chapter 2.

3.2 Numerical Validation

The numerical models of the flow fields in the front and in the back of the structure are validated separately. The numerical models of free standing structure and flow field in the back of the structure are the same as those developed in a previous work [58]. The numerical models have been validated previously. The 2-D numerical model simulating the interactions between a blast wave and a fixed V-shaped structure is validated by comparing the numerical results with the analytical solutions available in the literature.

At an incident angle of 0°, a normal reflection is produced. The reflected overpressure can be expressed in terms of the Mach number M_y, written as [5]

$$p_r = \frac{(3\gamma - 1)M_y^2 + (3 - \gamma)}{(\gamma - 1)M_y^2 + 2} p_s \tag{3.27}$$

where

$$p_s = \frac{2\gamma\left(M_y^2 - 1\right)}{\gamma + 1} p_0$$

where p_r is the reflected overpressure, and p_s is the incident overpressure.

When a blast wave impacts an inclined surface, oblique reflection will occur. The schematic diagram of oblique reflection is given in Figure 3.3. Figure 3.3 illustrates for an incident blast wave at M_y with an angle of incidence β. The corresponding reflected blast wave is at M_r and an angle of reflection δ. Analysis of the oblique reflection proceeds most conveniently by consideration of its steady-flow counterpart, shown in Figure 3.4. Entering stream velocity u_1 in Region I parallels the inclined surface. The stream in Region I passes through the incident blast wave at incident angle β into Region II, and is deflected at angle θ toward the incident blast wave. The stream in Region II then undergoes a reflected blast wave at incident angle β_2 and is deflected at the same angle θ towards the reflected blast wave, so that the stream in Region III parallels the inclined surface again. It should be noted that the deflection angle of the reflected blast wave equals but opposes that of the incident blast wave.

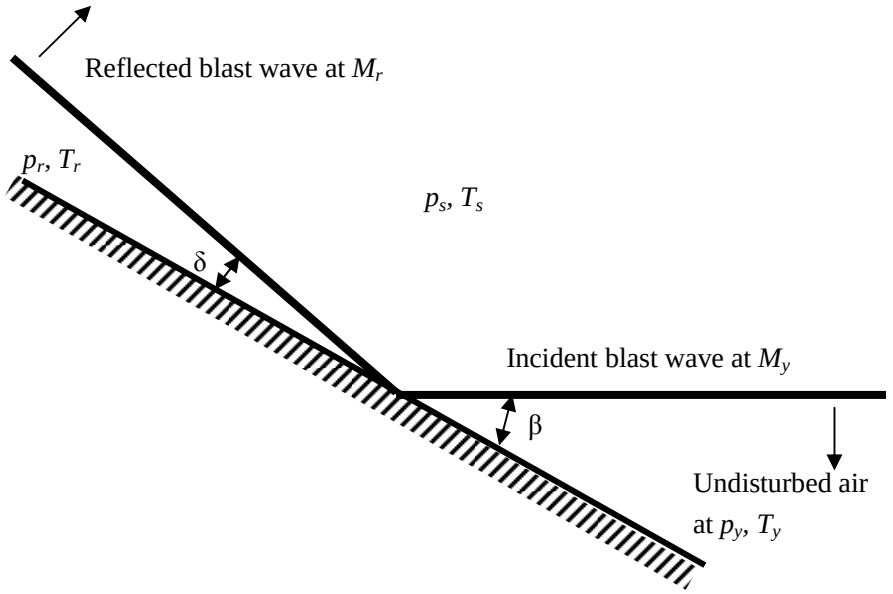

Figure 3.3: Oblique reflection of blast wave with angle of incidence β and angle of reflection δ

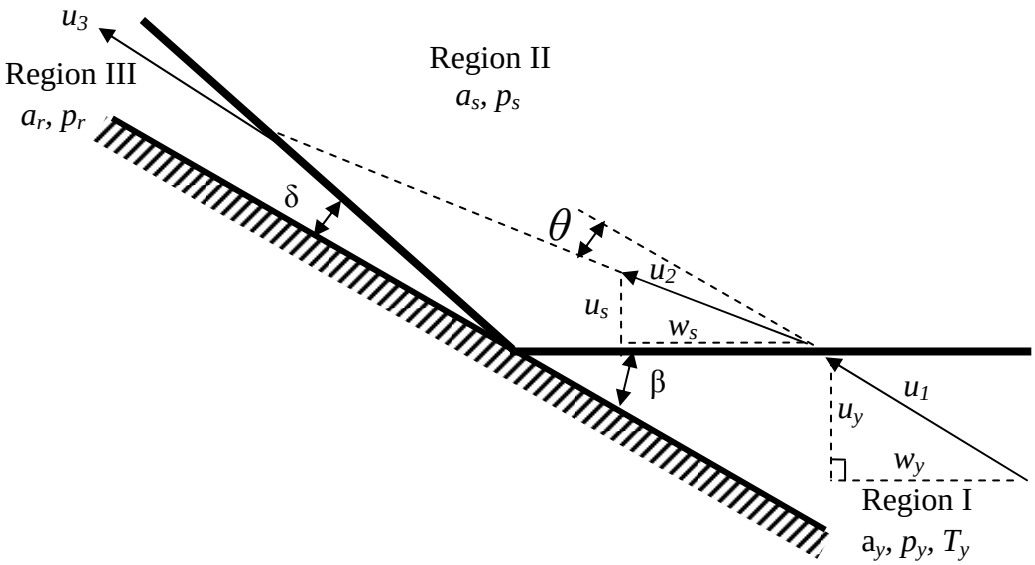

Figure 3.4: Steady flow counterpart of oblique reflection

For oblique reflection with given incident Mach number M_y and incident angle β, the reflected overpressure is given by [5]

$$p_r = \frac{\left(7M_r^2 - 1\right)\left(7M_y^2 - 1\right) - 36}{42\left(M_y^2 - 1\right)} p_s \tag{3.28}$$

where M_r is Mach number for the reflected blast wave, given by

$$M_r = M_2 \sin\beta_2 \tag{3.29}$$

where M_2 is the Mach number for the second stream in the region between the incident blast wave and the reflected blast wave, and can be determined using the equation

$$\left[M_2 \sin\left(\beta - \theta\right)\right]^2 = \frac{2 + \left(\gamma - 1\right)\left(M_1 \sin\beta\right)^2}{2\gamma\left(M_1 \sin\beta\right)^2 - \left(\gamma - 1\right)} \tag{3.30}$$

where θ is the stream deflection angle, given by

$$\frac{\tan\left(\beta - \theta\right)}{\tan\beta} = \frac{2 + \left(\gamma - 1\right)\left(M_1 \sin\beta\right)^2}{\left(\gamma + 1\right)\left(M_1 \sin\beta\right)^2} \tag{3.31}$$

Here M_1 is Mach number for the initial stream in the undisturbed region, which can be found from M_y and the geometry of Figure 3.4 as

$$M_1 = M_y / \sin\beta \tag{3.32}$$

Here β_2 is the incident angle between the second stream and the reflected blast wave, given by

$$\frac{\tan\left(\beta_2 - \theta\right)}{\tan\beta_2} = \frac{2 + \left(\gamma - 1\right)\left(M_2 \sin\beta_2\right)^2}{\left(\gamma + 1\right)\left(M_2 \sin\beta_2\right)^2} \tag{3.33}$$

The angle β_2 can not be solved directly using the above Equation (3.33), and an iterative method must be adopted.

When the incident angle is greater than the transition angle $\beta_{\max}$, Mach Stem reflection will occur. The transition angle can be determined by an empirical equation [5],

$$\beta_{\max} = \frac{1.75}{\left(M_y - 1\right)} + 39 \tag{3.34}$$

where β_{max} is the transition angle in degrees. Generally, the transition angle is around 40°. For Mach stem reflection, the reflected overpressure near the surface immediately behind the Mach stem can be approximately determined by equation [5]

$$p_r = \frac{2\gamma\left(M_s^2 - 1\right)}{\gamma + 1} p_0 \tag{3.35}$$

where M_s is the Mach number for the Mach stem, given by

$$M_s = M_y / \sin\beta \tag{3.36}$$

The reflected overpressure p_r *vs.* time t is plotted in Figure 3.5. Uniform blast waves with Mach numbers of 2 and 10 are adopted for the inflow boundary. An incident angle of 0° is chosen to simulate normal reflection, incident angles of $10^{\circ}$and 30° are chosen to simulate oblique reflection, and incident angles of 50° and 70° are chosen to simulate Mach stem reflection. Numerical profiles are compared to the analytical solutions. Before the incident blast wave approaches and impacts a fixed V-shaped structure, the reflected overpressure is zero. Upon reaching the structure, the incident blast wave is reflected from the inclined reflecting surface. The numerical reflected overpressure increases gradually to a constant value and oscillates about the constant value. While the analytical blast wave front shows very steep change in pressure, the blast wave is smeared in the numerical results. This is due to the numerical dissipation inherent in the flux vector splitting scheme. As shown in Figure 3.5, the numerical results agree well with the analytical solutions. The maximum errors for all cases are within 2%.

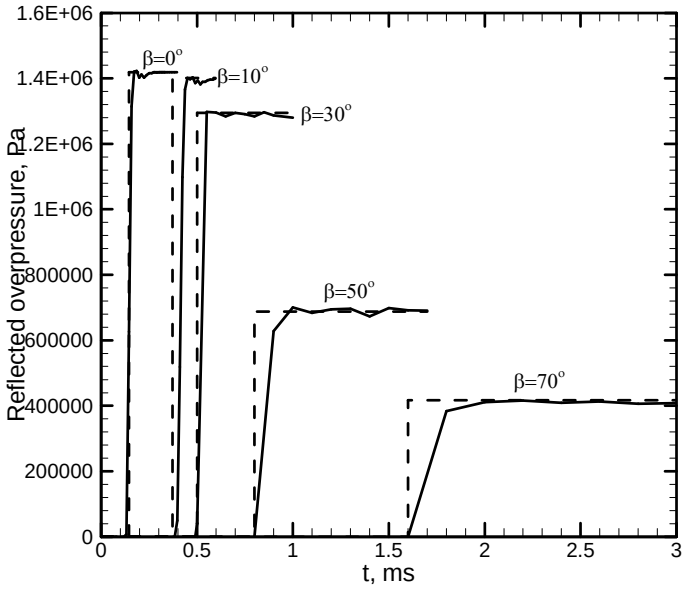

(a)

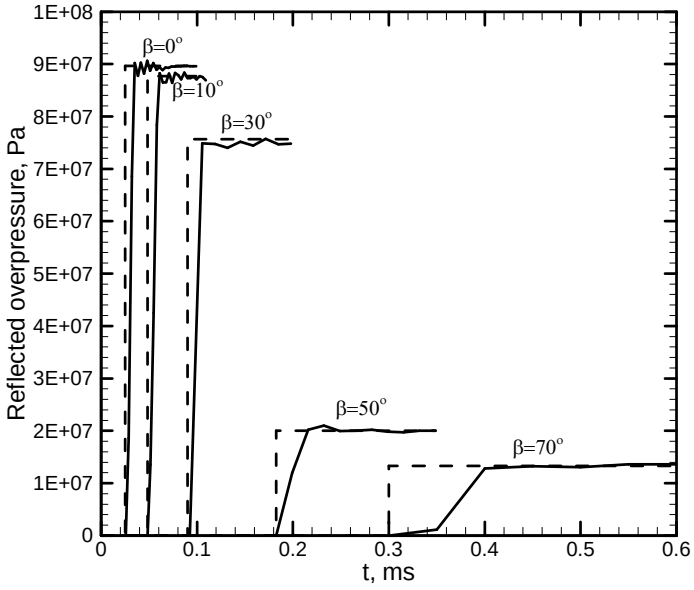

(b)

Figure 3.5: Comparison of numerical and analytical reflected overpressure profiles at different incident angles for (a) M_y=2; (b) M_y=10. (Dashed lines represent analytical solutions; Solid lines represent numerical results.)

It can be seen in Figure 3.5 that the reflected overpressure for Mach number of 10 is an order of magnitude larger than that for Mach number of 2. It shows that the reflected overpressure increases with the increase of blast intensity. For a given Mach number, the reflected overpressure decreases with the increase of incident angle. There is also a sharp drop of the reflected pressure for incident angles greater than the transition angle. It shows that the Mach stem reflection is much weaker than normal reflection and oblique reflection. However, the effects of Mach stem reflection in reducing blast wave impact decreases with the decrease of blast intensity.

The pressure contours of an exponential blast wave reflecting from a V-shaped structure at two incident angles are illustrated in Figure 3.6. At an incident angle of 30°, an oblique reflection is generated. The incident blast wave and the reflected blast wave intersect at the reflection point located on the inclined reflecting surface, which will move along the inclined reflecting surface with the propagation of the incident blast wave. At an incident angle of 50°, a Mach stem reflection occurs. The reflected blast wave and the incident blast wave intersect above the inclined reflecting surface and a third wavefront called the Mach stem is formed. The Mach stem is approximately perpendicular to the inclined reflecting surface. The incident blast front, the detached reflected blast front and the Mach stem wavefront intersect at a point, known as the triple point, which is located above the inclined reflecting surface. Figure 3.6 shows that the numerical model can successfully capture the different modes of blast wave reflection.

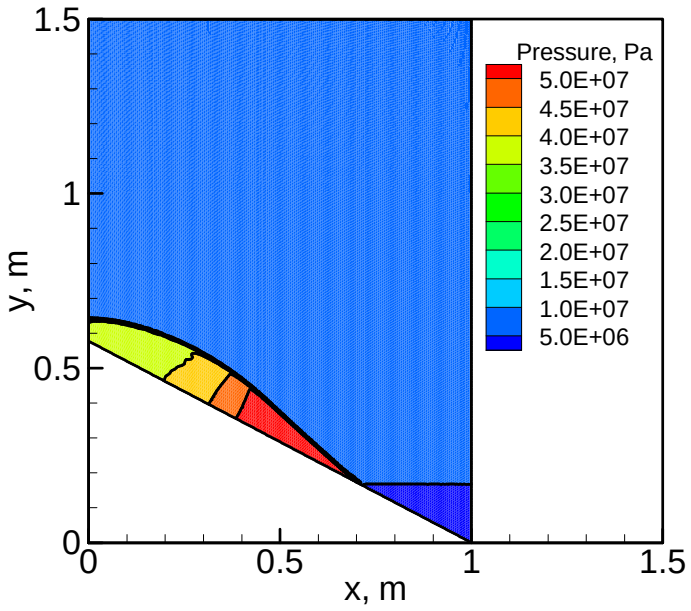

(a)

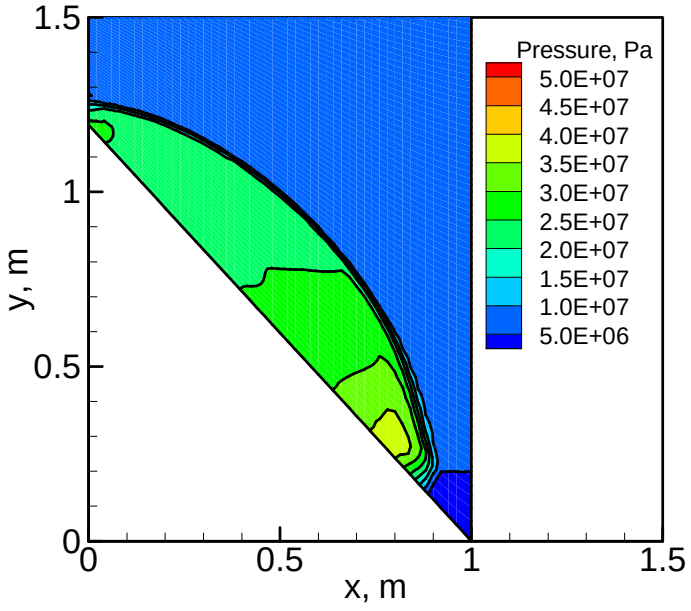

(b)

Figure 3.6: Pressure contours for (a) Oblique reflection at incident angle of 30°; (b) Mach stem reflection at incident angle of 50°

3.3 Results and Discussion

Simulations of a blast wave interacting with a V-shaped or a cone-shaped structure are conducted for different incident angles and masses of structure. The ratios of impulse transmitted to a structure (I_p) to the incident impulse (I_i) are compared between fixed and free-standing structures. The impulse is integral of pressure over time. Both uniform and exponential blast waves are simulated.

First, the numerical simulations of a uniform blast wave interacting with a structure are conducted. The uniform blast wave has a Mach number of 10 and an overpressure of 11.8 MPa. Five different incident angles of 0°, 10°, 30°, 50°, and 70° and three different masses of structure of 0.5 kg, 0.05 kg, and 0.005 kg are adopted. A stand-off distance from the structure of 1 m is adopted for the numerical simulation. The ratios of impulse I_p/I_i for a number of different scenarios are shown in Figure 3.7.

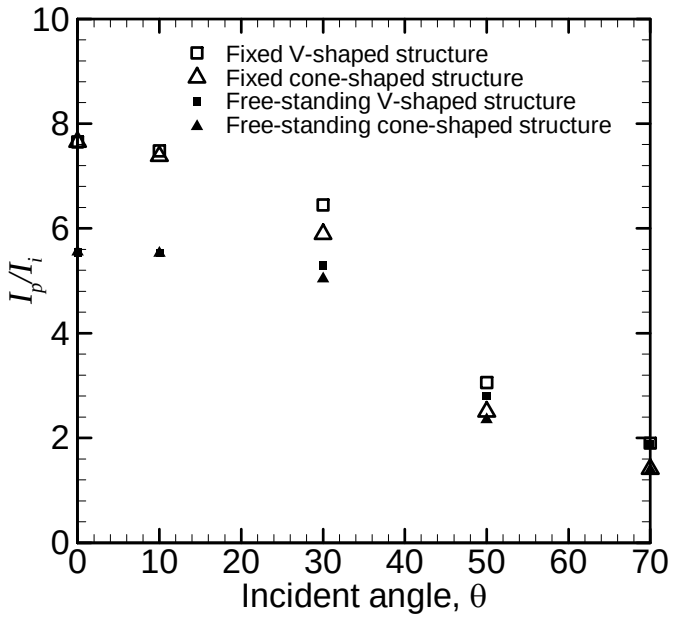
Fixed V-shaped structure
Fixed cone-shaped structure
Free-standing V-shaped structure
Free-standing cone-shaped structure
I_p/I_i
Incident angle, θ
0
2
4
6
8
10
0
10
20
30
40
50
60
70

(a)

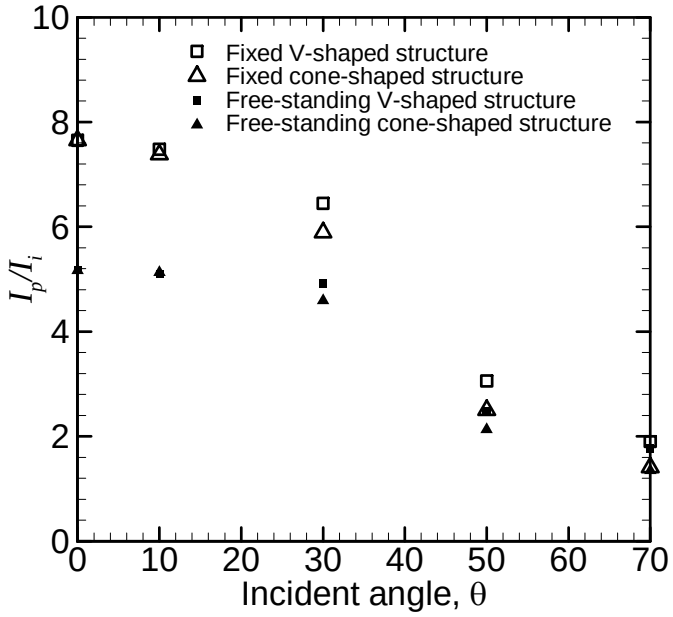
Fixed V-shaped structure
Fixed cone-shaped structure
Free-standing V-shaped structure
Free-standing cone-shaped structure
I_p/I_i
Incident angle, θ
0
2
4
6
8
10
0
10
20
30
40
50
60
70

(b)

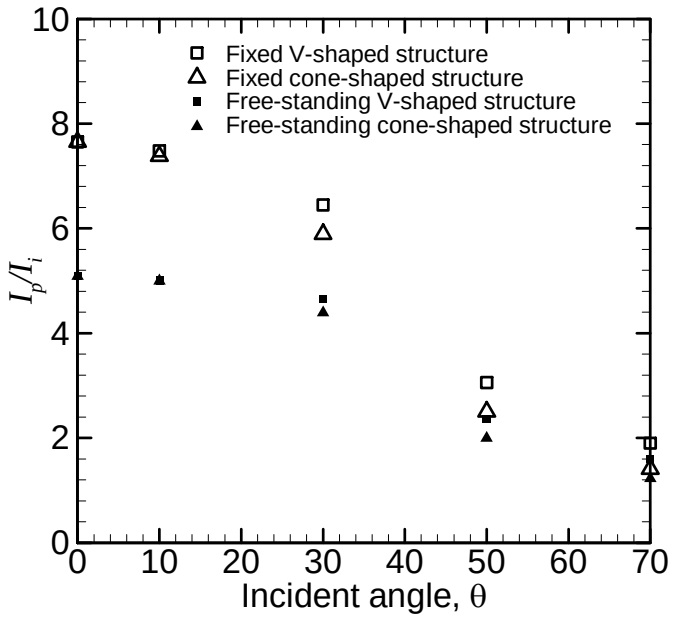

(c)

Figure 3.7: Ratio of impulse for uniform blast wave impacting structures with masses of (a) 0.5 kg, (b) 0.05 kg and (c) 0.005 kg at different incident angles

It can be seen from Figure 3.7 that the ratio of impulse decreases with the increase of incident angle. At an incident angle of 0°, normal reflection occurs. The ratios of impulse I_p/I_i for fixed V-shaped and cone-shaped structures are the same. At incident angles of 10° and 30°, the ratios of impulse I_p/I_i for fixed V-shaped and cone-shaped structures are around 90% of that for fixed flat structures, as shown in Figure 3.7. This is consistent with the fact that the impulse is an integral of pressure over time and oblique reflection only results in slight decrease of the reflected pressure. At incident angles of 50° and 70°, the ratios of impulse I_p/I_i for fixed V-shaped and cone-shaped structures decrease to below 50% of that for fixed flat structure. Because the incident angles are greater than the transition angle, Mach stem reflection occurs for both structures. The Mach stem

reflection results in significant decrease of reflected pressure, as well as the ratio of impulse I_p/I_i.

It can be seen in Figure 3.7 that the ratio of impulse I_p/I_i for a fixed cone-shaped structure is less than that for a fixed V-shaped structure, provided that the incident angle and the mass of the structure are the same. It implies that the impulse transmitted to a fixed cone-shaped structure is less than that to a fixed V-shaped structure. The blast wave loading on the cone-shaped structure is diverted sideways radially outward, while the blast wave loading on the V-shaped structure is diverted sideways only in the x-y plane. It is therefore expected that a cone-shaped structure is more effective in reducing blast wave impact than a V-shaped structure.

It can be seen in Figure 3.7 that the ratio of impulse I_p/I_i for a free-standing structure is significantly less than that for the corresponding fixed structure. For a free-standing structure, the impact of a blast wave will cause the structure to recede. The receding motion of the structure relieves the pressure experienced by the structure and results in a decrease in the impulse transmitted to the structure. It can also be seen in Figure 3.7 that the difference of the ratios of impulse I_p/I_i between a fixed and a free-standing structure decreases when incident angle increases. This is due to the decreased impulse transmitted to the structure, which is caused by oblique or Mach stem reflection. As the transmitted impulse decreases, the receding velocity of the structure decreases. Consequently, the effects of FSI in reducing blast wave impact decrease. This phenomenon is especially pronounced for incident angles greater than transition angle. As shown in Figure 3.7, the

impulse transmitted to a structure with incident angle of 70° is much less than that to a flat structure. This results in significant decrease of receding velocity, thus the effects of FSI become less pronounced. The difference of the ratios of impulse I_p/I_i between the fixed and free-standing structures is relatively small at incident angle of 70°.

The receding velocity of a structure increases when the mass of structure decreases. As a result, the effects of FSI in reducing blast wave impact increases. At an incident angle of 0°, the ratio of impulse I_p/I_i decreases only slightly with the decrease of mass, as shown in Figure 3.7. For strong incident blast wave, the structure is driven to very high receding velocity, which induces a strong shock wave in the back of the structure. When the shock wave strength in the back of the structure becomes comparable to the incident blast intensity, the effectiveness of FSI in reducing blast wave impulse diminishes. The ratio of impulse I_p/I_i reaches a plateau. At an incident angle of 70°, the ratio of impulse I_p/I_i decreases substantially with the significant decrease of mass, as shown in Figure 3.7. Because of the large incident angle, the impulse transmitted to the structure is much less than that to a flat structure. The smaller impulse transmitted to the structure results in a smaller receding velocity. Due to the relatively small receding velocity, the shock wave strength in the back of the structure is less than the incident blast intensity. This implies that the ratio of impulse I_p/I_i has not yet reached its plateau. As the mass of structure decreases, the receding velocity increases and the effects of FSI in blast wave mitigation increases.

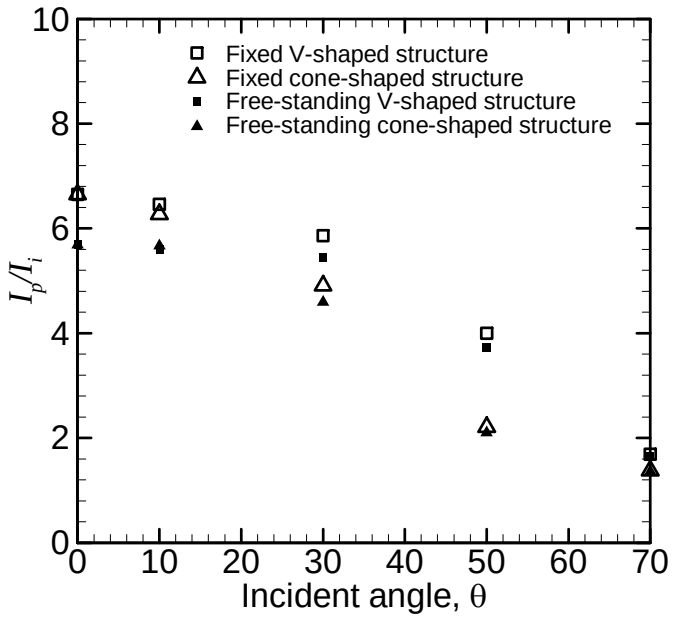
Fixed V-shaped structure
Fixed cone-shaped structure
Free-standing V-shaped structure
Free-standing cone-shaped structure
I_p/I_i
Incident angle, θ
0
2
4
6
8
10
0
10
20
30
40
50
60
70

(a)

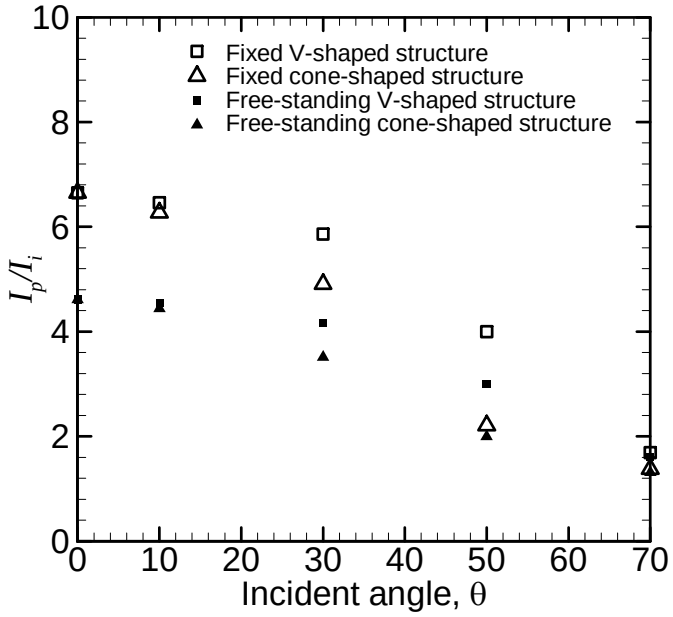
Fixed V-shaped structure
Fixed cone-shaped structure
Free-standing V-shaped structure
Free-standing cone-shaped structure
I_p/I_i
Incident angle, θ
0
2
4
6
8
10
0
10
20
30
40
50
60
70

(b)

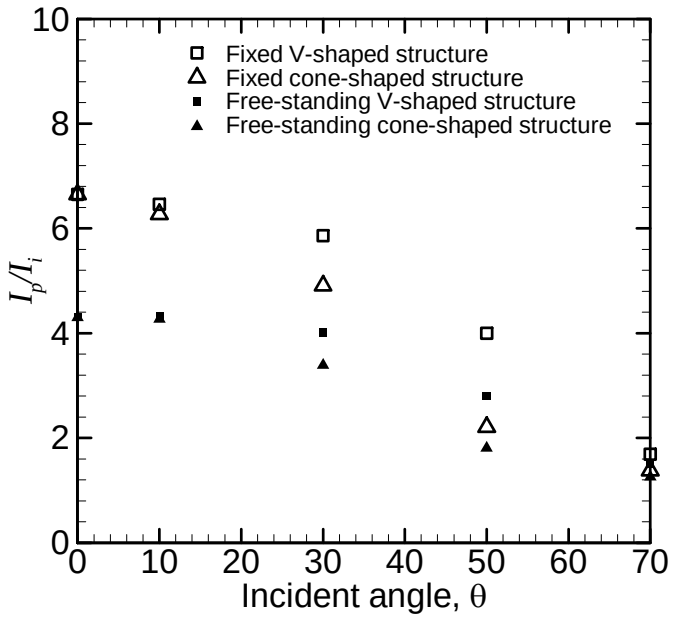

(c)

Figure 3.8: Ratio of impulse for exponential blast wave impacting structures with masses of (a) 0.5 kg, (b) 0.05 kg and (c) 0.005 kg at different incident angles

Second, the numerical simulations of an exponential blast wave interacting with a structure are conducted. The exponential blast wave has an initial peak Mach number of 10, an initial peak overpressure of 11.8 MPa and a decay time of 0.5 ms. The same incident angles, masses of structure, and stand-off distance as those used for the uniform blast wave are adopted. The ratios of impulse I_p/I_i for a number of different scenarios are shown in Figure 3.8.

The initial peak overpressure of exponential and uniform blast waves is the same. Since the overpressure of exponential blast wave decays with time, the reflection coefficient for a fixed flat structure decreases with the decrease of blast intensity. As expected, the ratios of impulse I_p/I_i for the exponential blast wave at incident angles of 0°,

10° and 30° are less than those for the uniform blast wave. At an incident angle of 50°, it is found that the ratios of impulse I_p/I_i for the fixed structures decrease gradually, while the corresponding ratios drop significantly in Figure 3.7. It is due to the decrease of blast intensity for exponential blast wave. The effects of Mach stem reflection in reducing blast wave impulse decreases with the decrease of blast intensity.

At a given incident angle and mass of structure, it can be seen that the difference of ratios of impulse I_p/I_i between a fixed and a free-standing structure for exponential blast wave is less than that for uniform blast wave. The decrease of blast intensity results in the reduced incident impulse and the decreased impulse transmitted to the structure. This results in relatively small receding velocity of structure. As a result, the effects of FSI in reducing blast wave impact decreases with the decrease of incident impulse. Figure 3.8 also shows that the ratio of impulse I_p/I_i decreases significantly with the decrease of mass at an incident angle of 0°. Because the exponential blast wave results in smaller receding velocity than that for uniform blast wave, this implies smaller shock wave strength in the back of the structure. Therefore, the ratio of impulse I_p/I_i has not yet reached its plateau. As the mass of structure decreases, the receding velocity increases and the effects of FSI in blast wave mitigation increases. At an incident angle of 70°, it can be seen that the difference of ratios of impulse I_p/I_i between a fixed and a free-standing structure is negligible. The exponential blast wave and large incident angle significantly decrease the impulse transmitted to the structure, which results in substantially smaller receding velocity. The effects of FSI in reducing blast wave impact are thus diminished.

3.4 Conclusions

A 2-D numerical model simulating interactions between a blast wave and a V-shaped or a cone-shaped structure has been developed in this study. The numerical model is validated by comparing numerical results with analytical solutions available in the literature for uniform blast waves. Numerical simulations of both uniform and exponential blast waves interacting with structures are conducted for different incident angles and different masses of structure. The oblique and Mach stem reflections reduce the blast wave impact. As a result, the ratios of impulse I_p/I_i for V-shaped and cone-shaped structures decrease with the increase of incident angle. The reduction in the ratios of impulse is especially pronounced for mach stem reflection. Due to the structural characteristics, a cone-shaped structure is more effective in reducing blast wave impact than a V-shaped structure.

The effects of FSI between a blast wave and a free-standing structure in reducing blast wave impact are investigated. The effects of FSI are dependent on the incident blast wave and mass of structure. With the increase of incident impulse or decrease of mass of structure, the effects of FSI increase. The effects of FSI are also affected by oblique and Mach stem reflections. With the increase of incident angle, the impulse transmitted to a structure decreases. As a result, the receding velocity of the structure decreases, the effects of FSI in reducing blast wave impact decreases as well. The FSI coupled with oblique or Mach stem reflections improves the blast wave mitigation.

CHAPTER 4

CONCLUSIONS

The blast waves not only incapacitate military and civilian personnel, but also damages buildings, vehicles, and other properties. Numerous studies have been made in this area to investigate the response of structures and behavior of blast waves when blast waves impact structures and to investigate the strategies to mitigate blast wave impact as well. In previous studies, the fluid structure interactions (FSI) between blast waves and structures are simplified. This dissertation presents the effort in modeling and simulation of the complicated interactions between blast waves and structures, which include fixed and free-standing flat, V-shaped and cone-shaped structures. The objective is to understand the FSI and reflection behavior of blast waves and to probe the effects of FSI coupled with oblique or Mach stem reflections in blast wave mitigation. Therefore, the models developed can provide insight into the design of optimal structures to mitigate blast wave impact.

Throughout this dissertation, both uniform and exponential blast waves are simulated. Overpressure profile is used, while the other primitive variables such as velocity, temperature and density are absolute values.

The accomplishments in the present research can be summarized as follows: First, a 1-D numerical model of the FSI between a blast wave and a free-standing plate in highly

compressible medium is developed to investigate the effects of FSI in blast wave mitigation. The numerical approach treats the FSI problem in a coupled manner by coupling the flow fields on both sides of a free-standing plate through the receding motion of the plate. Both the blast wave reflection in front of the plate and the shock wave induced in the back of the plate are considered in the model. The reflection coefficient for different plate thicknesses at different uniform incident blast intensities is investigated. For an exponential blast wave, the reflection coefficient can not be applied as both the incident pressure and reflected pressure vary with time. Therefore, the ratio of impulse is studied for the exponential blast wave. The ratios of impulse with and without resistance caused by the shock wave formation in the back of a free-standing plate are compared for different blast intensities at different plate thicknesses. The effectiveness of FSI in blast wave mitigation increases as the thickness of a free-standing plate decreases. However, the effectiveness reaches a plateau after the thickness decreases beyond a critical value. The results show that the resistance in the back of a free-standing plate plays an important role in the FSI, especially for relatively light plates. Therefore, to accurately model the FSI problem, it should be treated in a coupled manner. Numerical investigation of the FSI between a blast wave and a free-standing plate also reveals that the ratio of impulse is also highly dependent on the incident blast intensity and impulse.

Second, 2-D numerical model simulating interactions between a blast wave and a V-shaped or a cone-shaped structure is developed to investigate the effects of FSI coupled with oblique or Mach stem reflection in blast wave mitigation. Numerical

simulations of both uniform and exponential blast waves interacting with structures are conducted for different incident angles and different masses of structure. Ratios of impulse for uniform and exponential blast waves impacting structures with different masses at different incident angles are investigated. As the oblique and Mach stem reflections reduce blast wave impact, the ratios of impulse for V-shaped and cone-shaped structures decrease with the increase of incident angle. Due to the structural characteristics, a cone-shaped structure is more effective in reducing blast wave impact than a V-shaped structure. The effects of FSI are dependent on the incident blast wave and mass of structure. With the increase of incident impulse or decrease of mass of structure, the effects of FSI increase. The effects of FSI are also affected by oblique and Mach stem reflections. With the increase of incident angle, the impulse transmitted to a structure decreases. As a result, the receding velocity of the structure decreases, the effects of FSI in reducing blast wave impact decreases as well. The FSI coupled with oblique or Mach stem reflections improves the blast wave mitigation.

CHAPTER 5

FUTURE WORK

The research work in this dissertation treats a structure subjected to a blast wave as a rigid body. The effects of deformation and stress-wave propagation within the structure are neglected. In reality, the structure will deform more or less under the action of blast wave impact. As discussed earlier, the FSI problem is characterized by the coupling of the behavior of fluid surrounding the structure and the resulting motion of the structure. Further investigation of FSI problem, including the effects of deformation and stress-wave propagation within the structure, is important.

The FSI concepts have the potential to be applied to structural designs, such as sandwich panels made of various materials and core topologies. There have been many studies involving the resistance against blast wave of sandwich structures. It has been found that the sandwich structures have a higher shock resistance than monolithic structures of equal mass. In this dissertation, the monolithic V-shaped and cone-shaped structures are studied. In order to improve the effectiveness of V-shaped and cone-shaped structures in blast wave mitigation, sandwich V-shaped and cone-shaped structures can be designed using the FSI concepts. Further investigation of sandwich structures is useful.

As mentioned in chapter 3, a cone-shaped structure is more effective in blast wave mitigation than a V-shaped structure. This demonstrates that the shape of structure has

influence in blast wave mitigation. Further investigation of other shaped structures, which are beneficial to divert reflected blast wave sideways, may be considered.

REFERENCES

[1] N. Kambouchev, L. Noels and R. Radovitzky, Nonlinear compressibility effects in fluid-structure interaction and their implications on the air-blast loading of structures, *Journal of Applied Physics*, Vol. 100, No. 6, 063519, 2006.

[2] N. Kambouchev, L. Noels and R. Radovitzky, Numerical simulation of the fluid-structure interaction between air blast waves and free-standing plates, *Computers and Structures*, Vol. 85, pp. 923-931, 2007.

[3] N. Kambouchev, R. Radovitzky and L. Noels, Fluid-structure interaction effects in the dynamic response of free-standing plates to uniform shock loading, *Journal of Applied Mechanics*, Vol. 74, No. 5, pp. 1042-1045, 2007.

[4] N. Kambouchev, Analysis of blast mitigation strategies exploiting fluid-structure interaction, Ph.D. Thesis, *Massachusetts Institute of Technology*, 2007.

[5] G. F. Kinney and K. J. Graham, Explosive shocks in air, Springer-Verlag New York Inc., second edition, 1985.

[6] J. A. Main and G. A. Gazonas, Uniaxial crushing of sandwich plates under air blast: Influence of mass distribution, *International Journal of Solids and Structures*, Vol. 45, pp. 2297-2321, 2008.

[7] H. S. Turkmen and Z. Mecitoglu, Nonlinear structural response of laminated composite plates subjected to blast loading, *AIAA Journal*, Vol. 37, No. 12, pp. 1639-1647, 1999.

[8] N. S. Rudrapatna, R. Vaziri and M. D. Olson, Deformation and failure of blast-loaded square plates, *International Journal of Impact Engineering*, Vol. 22, No. 4, pp. 449-467, 1999.

[9] M. S. Chafi, G. Karami and M. Ziejewski, Numerical analysis of blast-induced wave propagation using FSI and ALE multi-material formulations, *International Journal of Impact Engineering*, Vol. 36, pp. 1269-1275, 2009.

[10] A. Neuberger, S. Peles and D. Rittel, Scaling the response of circular plates subjected to large and close-range spherical explosions. Part I: Air-blast loading, *International Journal of Impact Engineering*, Vol. 34, pp. 859-873, 2007.

[11] E. Alpman, L. N. Long, C. C. Chen and D. G. Linzell, Prediction of blast loads on a deformable steel plate using Euler equations, Collection of Technical Papers-18th AIAA Computational Fluid Dynamics Conference, Vol. 2, pp. 1289-1301, 2007.

[12] H. S. Turkmen, Structural response of laminated composite shells subjected to blast loading: comparison of experimental and theoretical methods, *Journal of Sound and Vibration*, Vol. 249, No. 4, pp. 663-678, 2002.

[13] M. S. Hoo Fatt, Rigid-plastic deformation of a ring-stiffened shell under blast loading, *Journal of Pressure Vessel Technology*, Vol. 119, No. 4, pp. 467-474, 1997.

[14] D. Redekop, Dynamic response of a toroidal shell panel to blast loading, *Computers & Structures*, Vol. 51, pp. 235-239, 1994.

[15] K. V. Subramaniam, W. Nian and Y. Andreopoulos, Blast response simulation of an elastic structure: Evaluation of the fluid-structure interaction effect, *International*

Journal of Impact Engineering, Vol. 36, pp. 965-974, 2009.

[16] S. Chun, H. Kapoor and R. K. Kapania, Nonlinear fluid-structure interaction of flexible shelters under blast loading, 46th AIAA/ASME/ASCE/AHS/ASC Structures, Structural Dynamics & Materials Conference, AIAA, Austin, TX, pp. 2005-2176, Apr 18-21 2005.

[17] K. Lee, T. Kim and J. Kim, Local response of W-shaped steel columns under blast loading, *Structural Engineering and Mechanics*, Vol. 31, No. 1, pp. 25-38, 2009.

[18] R. Houlston and J. E. Slater, Damage analysis with ADINA of naval panels subjected to a confined air-blast wave, *Computers and Structures*, Vol.47, No. 4-5, pp. 629-639, 1993.

[19] C. Y. Tham, Numerical simulation on the interaction of blast waves with a series of aluminum cylinders at near-field, *International Journal of Impact Engineering*, Vol. 36, pp. 122-131, 2009.

[20] F. Marconi, Investigation of the interaction of a blast wave with an internal structure, *AIAA Journal*, Vol. 32, No. 8, pp. 1561-1567, 1994.

[21] I. D. Elgy, D. J. Pope and I. M. Pickup, A study of combined particle and blast wave loading of structures, *Journal de Physique IV*, Vol. 134, pp. 467-471, 2006.

[22] R. W. McCoy and C. T. Sun, Fluid-structure interaction analysis of a thick-section composite cylinder subjected to underwater blast loading, *Composite Structures*, vol. 37, No. 1, pp. 45-55, 1997.

[23] K. Cichocki, Effects of underwater blast loading on structures with protective

elements, *International Journal of Impact Engineering*, Vol. 22, No. 6, pp. 609-617, 1999.

[24] H. D. Espinosa, S. Lee and N. Moldovan, A novel fluid structure interaction experiment to investigate deformation of structural elements subjected to impulsive loading, *Experimental Mechanics*, Vol. 46, pp. 805-824, 2006.

[25] C. H. Tai, J. T. Teng, S. W. Lo and C. W. Liu, A three-dimensional numerical investigation into the interaction of blast waves with bomb shelters, *JSME International Journal Series B,* Vol. 48, No. 4, pp. 820-829, 2005.

[26] Y. Shi, H. Hao and Z. Li, Numerical simulation of blast wave interaction with structure columns, *Shock Waves*, Vol. 17, pp. 113-133, 2007.

[27] J.Y. Yang, Y. Liu and H. Lomax, Computation of shock wave reflection by circular cylinders, *AIAA journal*, Vol. 25, No. 5, pp. 683-689, 1987.

[28] K. Takayama and H. Sekiquchi, Formation and diffraction of spherical shock waves in a shock tube, *Reports of the Institute of High Speed Mechanics*, Vol. 43, pp. 89-119, 1981.

[29] J. M. Dewey and D. J. McMillin, An analysis of the particle trajectories in spherical blast waves reflected from real and ideal surfaces, *Canadian Journal of Physics*, Vol. 59, No. 10, pp. 1380-1390, 1981.

[30] S. M. Liang, J. L. Hsu and J. S. Wang, Numerical study of cylindrical blast-wave propagation and reflection, *AIAA Journal*, Vol. 39, No. 6, pp. 1152-1158, 2001.

[31] S. M. Liang, J. S. Wang and H. Chen, Numerical study of spherical blast-wave

propagation and reflection, *Shock Waves*, Vol. 12, pp. 59-68, 2002.

[32] P. Colella, R. E. Ferguson, H. M. Glaz and A. L. Kuhl, Mach reflection from HE-driven blast wave, Proceeding of 10th ICDERES, Berkeley, California, Aug. 4-9 1985, AIAA Inc., New York, pp. 388-421, 1986.

[33] J. Olejniczak, M. J. Wright and G. V. Candler, Numerical study of inviscid shock interactions on double-wedge geometries, *Journal of Fluid Mechanics*, Vol. 352, pp. 1-25, 1997.

[34] G. Ben-dor, Interaction of a planar shock wave with a double-wedge-like structure, *AIAA Journal*, Vol. 30, No. 1, pp. 274-278, 1992.

[35] O. Igra, G. Hu, J. Falcovitz and B. Y. Wang, Shock wave reflection from a wedge in a dusty gas, *International Journal of Multiphase Flow*, Vol. 30, pp. 1139-1169, 2004.

[36] O. Igra, G. Hu, J. Falcovitz and W. Heilig, Blast wave reflection from wedges, *Journal of Fluids Engineering*, Vol. 125, No. 3, pp. 510-519, 2003.

[37] K. Takayama, G. Ben-Dor and J. Gotoh, Regular to Mach reflection transition in truly nonstationary flows-influence of surface roughness, *AIAA Journal*, vol. 19, No. 9, pp. 1238-1240, 1981.

[38] T. A. Rose, P. D. Smith and G. C. Mays, Effectiveness of walls designed for the protection of structures against air blast from high explosives, *Proceedings of the Institution of Civil Engineers: Structures and Buildings*, Vol. 110, No. 1, pp. 78-85, 1995.

[39] T. A. Rose, P. D. Smith and G. C. Mays, Design charts relating to protection of structures against air blast from high explosives, *Proceedings of the Institution of Civil Engineers: Structures and Buildings*, Vol. 122, No. 2, pp. 186-192, 1997.

[40] T. A. Rose, P. D. Smith and G. C. Mays, Protection of structures against air blast using barriers of limited robustness, *Proceedings of the Institution of Civil Engineers: Structures and Buildings*, Vol. 128, No. 2, pp. 167-176, 1998.

[41] X.Q. Zhou and H. Hao, Prediction of airblast loads on structures behind a protective barrier, *International Journal of Impact Engineering*, Vol. 35, pp. 363-375, 2008.

[42] Z. Su, W. Peng, Z. Zhang, G. Gogos, R. Skaggs and B. Cheeseman, Numerical simulation of a novel blast wave mitigation device, *International Journal of Impact Engineering*, Vol. 35, No. 5, pp. 336-346, 2008.

[43] X. Qiu, V. S. Deshpande and N. A. Fleck, Dynamic response of a clamped circular sandwich plate subject to shock loading, *Journal of Applied Mechanics*, Vol. 71, pp. 637-645, 2004.

[44] X. Qiu, V. S. Deshpande and N. A. Fleck, Finite element analysis of the dynamic response of clamped sandwich beams subject to shock loading, *European Journal of Mechanics*, Vol. 22, No. 6, pp. 801-814, 2003.

[45] X. Qiu, V. S. Deshpande and N. A. Fleck, Impulsive loading of clamped monolithic and sandwich beams over a central patch, *Journal of the Mechanics and Physics of Solids*, Vol. 53, No. 5, pp. 1015-1046, 2005.

[46] A. Vaziri and J. W. Hutchinson, Metal sandwich plates subject to intense air shocks,

International Journal of Solids and Structures, Vol. 44, pp. 2021-2035, 2007.

[47] Z. Xue and J. W. Hutchinson, A comparative study of impulse-resistant metal sandwich plates, *International Journal of Impact Engineering*, Vol. 30, pp. 1283-1305, 2004.

[48] Z. Xue and J. W. Hutchinson, Preliminary assessment of sandwich plates subject to blast loads, *International Journal of Mechanical Sciences*, Vol. 45, pp. 687-705, 2003.

[49] E. Wang, N. Gardner and A. Shukla, The blast resistance of sandwich composites with stepwise graded cores, *International Journal of Solids and Structures*, Vol. 46, pp. 3492-3502, 2009.

[50] P. Qiao, M. Yang and F. Bobaru, Impact mechanics and high-energy absorbing materials: review, *Journal of Aerospace Engineering*, Vol. 21, No. 4, pp. 235-248, 2008.

[51] Y. Liang, A. V. Spuskanyuk, S. E. Flores, D. R. Hayhurst, J. W. Hutchinson, R. M. McMeeking and A. G. Evans, The response of metallic sandwich panels to water blast, *Journal of Applied Mechanics*, Vol. 74, pp. 81-99, 2007.

[52] N. A. Fleck and V. S. Deshpande, The resistance of clamped sandwich beams to shock loading, *Journal of Applied Mechanics*, Vo. 71, No. 3, pp. 386-401, 2004.

[53] M. T. Tilbrook, V. S. Deshpande and N. A. Fleck, Underwater blast loading of sandwich beams: Regimes of behavior, *International Journal of Solids and Structures*, Vol. 46, No. 17, pp. 3209-3221, 2009.

[54] W. Kyle Anderson, James L. Thomas and Bram Van Leer, Comparison of finite volume flux vector splitting for the Euler equations, *AIAA Journal*, Vol. 24, No. 9, pp. 1453-1460, 1986.

[55] Bram Van Leer, Flux-vector splitting for the Euler equations, *Lecture Notes in Physics*, Vol. 170, pp. 507-512, 1982.

[56] John D. Anderson, Modern compressible flow, McGraw-Hill Companies, Inc., third edition, 2003.

[57] Klaus A. Hoffnann and Steve T. Chiang, Computational fluid dynamics for engineers-Volume II, ISBN 0-9623731-7-6, 1993.

[58] W. Peng, Z. Zhang, G. Gogos and G. Gazonas, Fluid structure interactions for blast wave mitigation, 38th Fluid Dynamics Conference and Exhibit, Seattle, WA, AIAA 2008-4418, 2008.

[59] John C. Tannehill, Dale A. Anderson and Richard H. Pletcher, Computational fluid mechanics and heat transfer, Taylor & Francis, second edition, 1997.

[60] Klaus A. Hoffnann and Steve T. Chiang, Computational fluid dynamics for engineers-Volume I, ISBN 0-9623731-7-6, 1993.

APPENDIX A

RANKINE-HUGONIOT RELATIONS

Rankine-Hugoniot equations relate changes of thermodynamic variables across a normal shock wave, and these are physically independent of whether or not the shock is moving. It is convenient to utilize the shock plane itself as the reference datum for the study of normal shock, as illustrated schematically in Figure A.1.

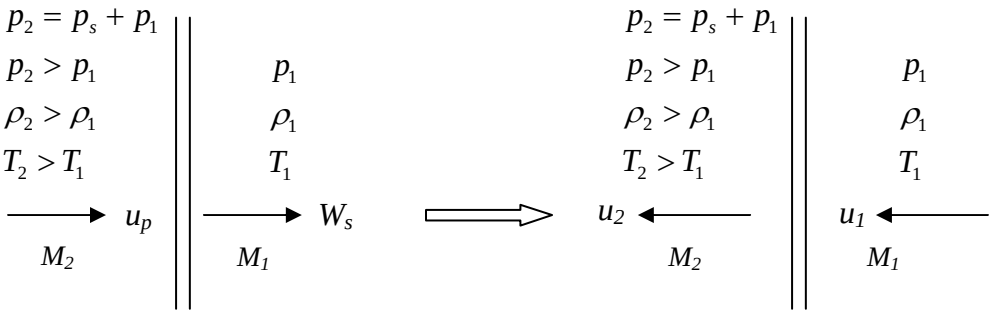

(a) moving normal shock wave (b) stationary normal shock wave

Figure A.1: Diagram of a normal shock wave. (a) moving normal shock wave; (b) stationary normal shock wave

A moving normal shock wave with a blast wave speed W_s is transformed to a stationary normal shock wave in steady flow. Medium enters from the right with stream velocity u_1 and decelerates to stream velocity u_2. The static pressure, density and temperature on both sides of the shock are not affected by the transformation. Additionally, they increase across the shock, as shown in Figure A.1. Here, p_1 and p_2 are

absolute pressure and p_s is overpressure. The fluid velocity behind the shock wave is u_p, which is equal to (u_1-u_2). u_1 is equal to W_s. M_1 and M_2 are Mach numbers ahead of the shock wave and behind the shock wave, respectively.

The density, velocity and temperature ratios can be expressed as a function of Mach number M_1, given by [56]

$$\frac{\rho_2}{\rho_1}=\frac{u_1}{u_2}=\frac{(\gamma+1)M_1^2}{2+(\gamma-1)M_1^2} \tag{A.1a}$$

$$\frac{T_2}{T_1}=\left[1+\frac{2\gamma}{\gamma+1}\left(M_1^2-1\right)\right]\left[\frac{2+(\gamma-1)M_1^2}{(\gamma+1)M_1^2}\right] \tag{A.1b}$$

For application to practical problems, it is often more convenient to use the absolute pressure ratio p_2/p_1 or the overpressure ratio p_s/p_1 as the basic independent variable. The absolute pressure ratio and the overpressure ratio can be expressed as a function of Mach number M_1, given by [56]

$$\frac{p_2}{p_1}=1+\frac{2\gamma}{\gamma+1}\left(M_1^2-1\right) \tag{A.2a}$$

$$\frac{p_s}{p_1}=\frac{2\gamma}{\gamma+1}\left(M_1^2-1\right) \tag{A.2b}$$

Therefore,

$$M_1^2=\left(\frac{p_2}{p_1}-1\right)\frac{\gamma+1}{2\gamma}+1 \tag{A.3a}$$

$$M_1^2=\frac{p_s}{p_1}\frac{\gamma+1}{2\gamma}+1 \tag{A.3b}$$

Substituting Equations (A.3a) and (A.3b) for Mach number M_1 into Equations (A.1a) and (A.1b):

$$\frac{\rho_2}{\rho_1}=\frac{u_1}{u_2}=\frac{1+\dfrac{\gamma+1}{\gamma-1}\dfrac{p_2}{p_1}}{\dfrac{\gamma+1}{\gamma-1}+\dfrac{p_2}{p_1}}=\frac{(\gamma+1)\dfrac{p_s}{p_1}+2\gamma}{(\gamma-1)\dfrac{p_s}{p_1}+2\gamma} \tag{A.4}$$

$$\frac{T_2}{T_1}=\frac{p_2}{p_1}\frac{\dfrac{p_2}{p_1}+\dfrac{\gamma+1}{\gamma-1}}{\dfrac{p_2}{p_1}\dfrac{\gamma+1}{\gamma-1}+1}=\left(\frac{p_s}{p_1}+1\right)\frac{\dfrac{p_s}{p_1}\dfrac{\gamma-1}{2\gamma}+1}{\dfrac{p_s}{p_1}\dfrac{\gamma+1}{2\gamma}+1} \tag{A.5}$$

The Equations (A.4) and (A.5) are the Rankine-Hugoniot relations, which give the density, velocity and temperature ratios across the shock wave as a function of the absolute pressure ratio and the overpressure ratio. Throughout this dissertation, the Rankine-Hugoniot relations through which the density, velocity and temperature ratios are related to the overpressure ratio are applied.

The Mach number of the shock wave is given by

$$M_1=\frac{W_s}{a_1}=\frac{u_1}{a_1} \tag{A.6}$$

which yields

$$u_1=M_1a_1 \tag{A.7}$$

Combining Equations (A.4) and (A.7), the fluid velocity behind the shock wave is

$$u_p=\frac{a_1}{\gamma}\left(\frac{p_2}{p_1}-1\right)\sqrt{\frac{\dfrac{2\gamma}{\gamma+1}}{\dfrac{\gamma-1}{\gamma+1}+\dfrac{p_2}{p_1}}}=a_1\left(\frac{(2/\gamma)\dfrac{p_s}{p_1}}{2\gamma\dfrac{p_1}{p_s}+(\gamma+1)}\right)^{1/2} \tag{A.8}$$

The Rankine-Hugoniot relations can be applied to the reflected shock wave and the induced shock wave as a normal shock wave impacts a free-standing plat. The diagram of

a normal shock wave impacting a free-standing plate is illustrated schematically in Figure A.2.

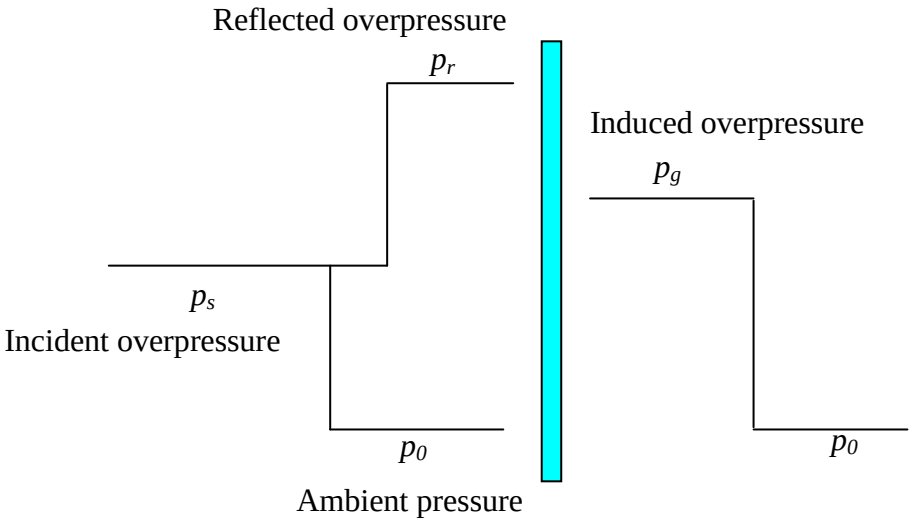

Figure A.2: Diagram of a normal shock wave impacting a free-standing plate

The overpressure of induced shock wave is related to the plate velocity u_p through Equation (A.8)

$$u_p = a_0 \left(\frac{(2/\gamma)\frac{p_g}{p_0}}{2\gamma \frac{p_0}{p_g} + (\gamma + 1)} \right)^{1/2} \tag{A.9}$$

For the reflected shock wave, W_r is the reflected blast wave speed, u_s is the fluid velocity behind the incident shock front, u_p is the plate velocity. Therefore, the stream velocity ahead of the reflected shock wave u_1 is (W_r+ u_s), and the stream velocity behind the reflected shock wave u_2 is (W_r+ u_p). The incident blast wave overpressure is p_s, and the reflected blast wave overpressure is p_r. The absolute pressure in front of the reflected shock wave p_1 is (p_s+p_0), and the absolute pressure behind the reflected shock wave p_2 is

(p_r+p_0). Applying Equation (A.4), we obtain

$$\frac{W_r + u_s}{W_r + u_p} = \frac{(\gamma+1)\dfrac{p_r - p_s}{p_s + p_0} + 2\gamma}{(\gamma-1)\dfrac{p_r - p_s}{p_s + p_0} + 2\gamma} \tag{A.10}$$

Here,

$$W_r = a_r M_r - u_s \tag{A.11}$$

Applying Equation (A.3b), the Mach number for the reflected blast wave, M_r, is given by

$$M_r = \sqrt{\left(\frac{\gamma+1}{2\gamma}\right)\left(\frac{p_r - p_s}{p_s + p_0}\right) + 1} \tag{A.12}$$

The speed of sound a_r is related to T_s, the temperature behind the incident shock front, through the equation

$$a_r = \sqrt{\gamma R T_s} \tag{A.13}$$

Applying Equation (A.5), T_s is given by

$$T_s = T_0\left[\left(\frac{\gamma-1}{2\gamma}\right)\frac{p_s}{p_0} + 1\right]\left(\frac{\dfrac{p_s}{p_0} + 1}{\left(\dfrac{\gamma+1}{2\gamma}\right)\dfrac{p_s}{p_0} + 1}\right) \tag{A.14}$$

For a free-standing plate of infinitesimal mass, p_g equals p_r. Combining Equations (A.9)-(A.14) yields a reflection coefficient p_r/p_s of 1.

APPENDIX

B

ELLIPTIC GRID GENERATION

B.1 Metrics and the Jacobian of Transformation

The independent variables in the physical domain (*x*, *y*) are transformed to a new set of independent variables in the transformed domain (ξ, η), where

$$\xi = \xi(x, y) \tag{B.1a}$$

$$\eta = \eta(x, y) \tag{B.1b}$$

Equations (B.1a) and (B.1b) represent the transformation. The total differential of ξ and η are given by

$$d\xi = \xi_x dx + \xi_y dy \tag{B.2a}$$

$$d\eta = \eta_x dx + \eta_y dy \tag{B.2b}$$

Equations (B.2a) and (B.2b) can be written in a compact form as

$$\begin{bmatrix} d\xi \\ d\eta \end{bmatrix} = \begin{bmatrix} \xi_x & \xi_y \\ \eta_x & \eta_y \end{bmatrix} \begin{bmatrix} dx \\ dy \end{bmatrix} \tag{B.3}$$

In Equation (B.3), the terms involving the geometry of the grid, such as $\xi_x, \xi_y, \eta_x, \eta_y$ are called metrics. Reversing the role of independent variables in Equations (B.1a) and (B.1b), the inverse transformation is given by

$$x = x(\xi, \eta) \tag{B.4a}$$

$$y = y(\xi, \eta) \tag{B.4b}$$

Similarly, the following compact form can be obtained

$$\begin{bmatrix} dx \\ dy \end{bmatrix} = \begin{bmatrix} x_\xi & x_\eta \\ y_\xi & \mathrm{y}_\eta \end{bmatrix} \begin{bmatrix} d\xi \\ d\eta \end{bmatrix} \tag{B.5}$$

In Equation (B.5), the terms involving the geometry of the grid, such as $x_\xi, x_\eta, y_\xi, y_\eta$ are called inverse metrics. Solving Equation (B.5) for the right-hand column matrix, we have

$$\begin{bmatrix} d\xi \\ d\eta \end{bmatrix} = \begin{bmatrix} x_\xi & x_\eta \\ y_\xi & \mathrm{y}_\eta \end{bmatrix}^{-1} \begin{bmatrix} dx \\ dy \end{bmatrix} \tag{B.6}$$

Comparing Equations (B.3) and (B.6), we have

$$\begin{bmatrix} \xi_x & \xi_y \\ \eta_x & \eta_y \end{bmatrix} = \begin{bmatrix} x_\xi & x_\eta \\ y_\xi & y_\eta \end{bmatrix}^{-1} \tag{B.7}$$

Following the standard rules for creating the inverse of a matrix, Equation (B.7) is written as

$$\begin{bmatrix} \xi_x & \xi_y \\ \eta_x & \eta_y \end{bmatrix} = \frac{\begin{bmatrix} y_\eta & -x_\eta \\ -y_\xi & x_\xi \end{bmatrix}}{\begin{vmatrix} x_\xi & x_\eta \\ y_\xi & y_\eta \end{vmatrix}} \tag{B.8}$$

In Equation (B.8), the denominator determinant is defined as the Jacobian of the transformation, denoted by

$$J = \frac{\partial(x, y)}{\partial(\xi, \eta)} = \begin{vmatrix} x_\xi & x_\eta \\ y_\xi & y_\eta \end{vmatrix} \tag{B.9}$$

Comparing like elements of two matrices in Equation (B.8), we obtain the relationships for the direct metrics in terms of the inverse metrics, given by

$$\xi_x = \frac{1}{J} y_\eta \tag{B.10a}$$

$$\eta_x = -\frac{1}{J} y_\xi \tag{B.10b}$$

$$\xi_y = -\frac{1}{J} x_\eta \tag{B.10c}$$

$$\eta_y = \frac{1}{J} x_\xi \tag{B.10d}$$

B.2 Elliptic Grid Generation

For a blast wave impacting a V-shaped or a cone-shaped structure, it is difficult to develop finite difference equations in the physical domain. It is necessary to employ a general mapping to transform the irregular physical domain into a rectangular computational domain. As this physical domain has well-defined geometric boundaries, elliptic grid generator is used. The mapping is a one-to-one correspondence between the rectangular grid in the computational domain and the curvilinear grid in the physical domain. Complex boundaries are easily treated with the elliptic grid generator. The resulting grid from the elliptic grid generator is smooth. The mapping is constructed by specifying the desired grid points (x, y) on the boundary of the physical domain with the interior point distribution determined through the solution of the simplest elliptic equations, Laplace's equations, which are written as [59]

$$\xi_{xx} + \xi_{yy} = 0 \tag{B.11a}$$

$$\eta_{xx} + \eta_{yy} = 0 \tag{B.11b}$$

In the above Equations (B.11a) and (B.11b), ξ and η are dependent variables, while x and y are independent variables. The uniform grid in the computational domain is prescribed. In order to solve the (x, y) location of interior grid points in the physical domain, the above Equations (B.11a) and (B.11b) need to be transformed to computational domain by interchanging the roles of the independent and dependent variables.

To determine the second-order derivatives, ξ_{xx}, ξ_{yy}, η_{xx}, and η_{yy}, Equations (B.10a)-(B.10d) are applied.

$$\begin{aligned}\xi_{xx} &= \frac{\partial}{\partial x}(\xi_x) = \frac{\partial}{\partial x}\left(\frac{1}{J} y_\eta\right) \\ &= \frac{1}{J^3}\left[-(y_\eta)^3 x_{\xi\xi} + 2(y_\eta)^2 y_\xi x_{\xi\eta} - y_\eta (y_\xi)^2 x_{\eta\eta} - 2 y_\xi x_\eta y_\eta y_{\xi\eta} + x_\eta (y_\eta)^2 y_{\xi\xi} + (y_\xi)^2 x_\eta y_{\eta\eta}\right]\end{aligned} \tag{B.12a}$$

$$\begin{aligned}\xi_{yy} &= \frac{\partial}{\partial y}(\xi_y) = \frac{\partial}{\partial y}\left(-\frac{1}{J} x_\eta\right) \\ &= \frac{1}{J^3}\left[(x_\eta)^3 y_{\xi\xi} - 2(x_\eta)^2 x_\xi y_{\xi\eta} - y_\eta (x_\xi)^2 x_{\eta\eta} + 2 x_\xi x_\eta y_\eta x_{\xi\eta} - y_\eta (x_\eta)^2 x_{\xi\xi} + (x_\xi)^2 x_\eta y_{\eta\eta}\right]\end{aligned} \tag{B.12b}$$

$$\begin{aligned}\eta_{xx} &= \frac{\partial}{\partial x}(\eta_x) = \frac{\partial}{\partial x}\left(-\frac{1}{J} y_\xi\right) \\ &= \frac{1}{J^3}\left[(y_\xi)^3 x_{\eta\eta} - 2(y_\xi)^2 y_\eta x_{\xi\eta} + y_\xi (y_\eta)^2 x_{\xi\xi} + 2 y_\xi x_\xi y_\eta y_{\xi\eta} - x_\xi (y_\eta)^2 y_{\xi\xi} - (y_\xi)^2 x_\xi y_{\eta\eta}\right]\end{aligned} \tag{B.12c}$$

$$\begin{aligned}\eta_{yy} &= \frac{\partial}{\partial y}(\eta_y) = \frac{\partial}{\partial y}\left(\frac{1}{J} x_\xi\right) \\ &= \frac{1}{J^3}\left[-(x_\xi)^3 y_{\eta\eta} + 2(x_\xi)^2 x_\eta y_{\xi\eta} + y_\xi (x_\eta)^2 x_{\xi\xi} - 2 x_\xi x_\eta y_\xi x_{\xi\eta} + y_\xi (x_\xi)^2 x_{\eta\eta} - (x_\eta)^2 x_\xi y_{\xi\xi}\right]\end{aligned} \tag{B.12d}$$

Substituting Equations (B.12a)-(B.12d) into Equations (B.11a) and (B.11b) and

rearranging the sequence of terms, we have

$$\alpha x_{\xi\xi} - 2\beta x_{\xi\eta} + \gamma x_{\eta\eta} = 0 \tag{B.13a}$$

$$\alpha y_{\xi\xi} - 2\beta y_{\xi\eta} + \gamma y_{\eta\eta} = 0 \tag{B.13b}$$

where

$$\alpha = x_\eta^2 + y_\eta^2$$
$$\beta = x_\xi x_\eta + y_\xi y_\eta$$
$$\gamma = x_\xi^2 + y_\xi^2$$

The Equations (B.13a) and (B.13b) are the inverse of Laplace's Equations (B.11a) and (B.11b), with *x, y* as dependent variables. The (*x, y*) location of interior grid points in the physical domain as a function of the (ξ, η) location of the corresponding grid points in the computational domain can be calculated through the transformed Equations (B.13a) and (B.13b).

B.3 Finite Difference Formulations

The 2-D Equations (B.13a) and (B.13b) are solved by alternating-direction implicit (ADI) method, given by

$$\alpha \frac{x_{i-1,j} - 2x_{i,j} + x_{i+1,j}}{(\Delta\xi)^2} - 2\beta \frac{1}{4\Delta\xi\Delta\eta}\left(x_{i+1,j+1} + x_{i-1,j-1} - x_{i+1,j-1} - x_{i-1,j+1}\right) + \gamma \frac{x_{i,j-1} - 2x_{i,j} + x_{i,j+1}}{(\Delta\eta)^2} = 0 \tag{B.14a}$$

$$\alpha \frac{y_{i-1,j} - 2y_{i,j} + y_{i+1,j}}{(\Delta\xi)^2} - 2\beta \frac{1}{4\Delta\xi\Delta\eta}\left(y_{i+1,j+1} + y_{i-1,j-1} - y_{i+1,j-1} - y_{i-1,j+1}\right) + \gamma \frac{y_{i,j-1} - 2y_{i,j} + y_{i,j+1}}{(\Delta\eta)^2} = 0 \tag{B.14b}$$

where

$$\alpha = \left(\frac{x_{i,j+1} - x_{i,j-1}}{2\Delta\eta} \right)^2 + \left(\frac{y_{i,j+1} - y_{i,j-1}}{2\Delta\eta} \right)^2$$

$$\beta = \left(\frac{x_{i+1,j} - x_{i-1,j}}{2\Delta\xi} \right)\left(\frac{x_{i,j+1} - x_{i,j-1}}{2\Delta\eta} \right) + \left(\frac{y_{i+1,j} - y_{i-1,j}}{2\Delta\xi} \right)\left(\frac{y_{i,j+1} - y_{i,j-1}}{2\Delta\eta} \right)$$

$$\gamma = \left(\frac{x_{i+1,j} - x_{i-1,j}}{2\Delta\xi} \right)^2 + \left(\frac{y_{i+1,j} - y_{i-1,j}}{2\Delta\xi} \right)^2$$

The ADI scheme is solved in two steps. During the first step, with variables are implicit in *x* direction and explicit in *y* direction, a tridiagonal matrix is solved for *x* using Equation (B.14a) and a tridiagonal matrix is solved for *y* using Equation (B.14b) along each *i* row of grid points. During the second step, with variables are explicit in *x* direction and implicit in *y* direction, a tridiagonal matrix is solved for *x* using Equation (B.14a) and a tridiagonal matrix is solved for *y* using Equation (B.14b) along each *j* column of grid points. Repeat the two steps, until convergence is approached.

APPENDIX C

COORDINATE TRANSFORMATION

The 2-D Euler equations in cylindrical coordinates are written in vector form as [57]

$$\frac{\partial U}{\partial t}+\frac{\partial F}{\partial x}+\frac{\partial G}{\partial y}=S \tag{C.1}$$

When the governing equations are solved in the computational domain, they must be expressed in terms of the variables ξ and η. Therefore, the 2-D Euler equations in cylindrical coordinates are transformed from (x, y) to (ξ, η) as the new independent variables. The independent variables in the computational domain (ξ, η) are related to the independent variables in the physical domain (x, y) by the following equations

$$\xi=\xi(x,y) \tag{C.2a}$$

$$\eta=\eta(x,y) \tag{C.2b}$$

The chain rule of partial differentiation provides the following expressions

$$\frac{\partial U}{\partial t}+\frac{\partial F}{\partial \xi}\frac{\partial \xi}{\partial x}+\frac{\partial F}{\partial \eta}\frac{\partial \eta}{\partial x}+\frac{\partial G}{\partial \xi}\frac{\partial \xi}{\partial y}+\frac{\partial G}{\partial \eta}\frac{\partial \eta}{\partial y}=S \tag{C.3}$$

Multiplying both sides of Equation (C.3) by Jacobian J, we obtain

$$J\frac{\partial U}{\partial t}+J\frac{\partial F}{\partial \xi}\frac{\partial \xi}{\partial x}+J\frac{\partial F}{\partial \eta}\frac{\partial \eta}{\partial x}+J\frac{\partial G}{\partial \xi}\frac{\partial \xi}{\partial y}+J\frac{\partial G}{\partial \eta}\frac{\partial \eta}{\partial y}=JS \tag{C.4}$$

Now, considering the following relations:

$$\frac{\partial\left[JF\left(\frac{\partial\xi}{\partial x}\right)\right]}{\partial\xi} = J\frac{\partial F}{\partial\xi}\frac{\partial\xi}{\partial x} + F\frac{\partial\left[J\left(\frac{\partial\xi}{\partial x}\right)\right]}{\partial\xi} \tag{C.5}$$

Therefore, we have

$$J\frac{\partial F}{\partial\xi}\frac{\partial\xi}{\partial x} = \frac{\partial\left[JF\left(\frac{\partial\xi}{\partial x}\right)\right]}{\partial\xi} - F\frac{\partial\left[J\left(\frac{\partial\xi}{\partial x}\right)\right]}{\partial\xi} \tag{C.6}$$

Similarly,

$$J\frac{\partial F}{\partial\eta}\frac{\partial\eta}{\partial x} = \frac{\partial\left[JF\left(\frac{\partial\eta}{\partial x}\right)\right]}{\partial\eta} - F\frac{\partial\left[J\left(\frac{\partial\eta}{\partial x}\right)\right]}{\partial\eta} \tag{C.7}$$

$$J\frac{\partial G}{\partial\xi}\frac{\partial\xi}{\partial y} = \frac{\partial\left[JG\left(\frac{\partial\xi}{\partial y}\right)\right]}{\partial\xi} - G\frac{\partial\left[J\left(\frac{\partial\xi}{\partial y}\right)\right]}{\partial\xi} \tag{C.8}$$

$$J\frac{\partial G}{\partial\eta}\frac{\partial\eta}{\partial y} = \frac{\partial\left[JG\left(\frac{\partial\eta}{\partial y}\right)\right]}{\partial\eta} - G\frac{\partial\left[J\left(\frac{\partial\eta}{\partial y}\right)\right]}{\partial\eta} \tag{C.9}$$

Substitution of Equations (C.6)-(C.9) into Equation (C.4) and rearranging terms yields

$$J\frac{\partial U}{\partial t} + \frac{\partial\left[JF\left(\frac{\partial\xi}{\partial x}\right) + JG\left(\frac{\partial\xi}{\partial y}\right)\right]}{\partial\xi} + \frac{\partial\left[JF\left(\frac{\partial\eta}{\partial x}\right) + JG\left(\frac{\partial\eta}{\partial y}\right)\right]}{\partial\eta}$$
$$- F\left[\frac{\partial\left(J\frac{\partial\xi}{\partial x}\right)}{\partial\xi} + \frac{\partial\left(J\frac{\partial\eta}{\partial x}\right)}{\partial\eta}\right] - G\left[\frac{\partial\left(J\frac{\partial\xi}{\partial y}\right)}{\partial\xi} + \frac{\partial\left(J\frac{\partial\eta}{\partial y}\right)}{\partial\eta}\right] = JS \tag{C.10}$$

Applying Equations (B.10a)-(B.10d), we have

$$\frac{\partial\left(J\frac{\partial\xi}{\partial x}\right)}{\partial\xi}+\frac{\partial\left(J\frac{\partial\eta}{\partial x}\right)}{\partial\eta}=\frac{\partial\left(\frac{\partial y}{\partial\eta}\right)}{\partial\xi}+\frac{\partial\left(-\frac{\partial y}{\partial\xi}\right)}{\partial\eta}=0 \tag{C.11a}$$

$$\frac{\partial\left(J\frac{\partial\xi}{\partial y}\right)}{\partial\xi}+\frac{\partial\left(J\frac{\partial\eta}{\partial y}\right)}{\partial\eta}=\frac{\partial\left(-\frac{\partial x}{\partial\eta}\right)}{\partial\xi}+\frac{\partial\left(\frac{\partial x}{\partial\xi}\right)}{\partial\eta}=0 \tag{C.11b}$$

Therefore, we obtain

$$\frac{\partial(JU)}{\partial t}+\frac{\partial\left[JF\left(\frac{\partial\xi}{\partial x}\right)+JG\left(\frac{\partial\xi}{\partial y}\right)\right]}{\partial\xi}+\frac{\partial\left[JF\left(\frac{\partial\eta}{\partial x}\right)+JG\left(\frac{\partial\eta}{\partial y}\right)\right]}{\partial\eta}=JS \tag{C.12}$$

The transformed Euler Equation (C.12) in cylindrical coordinates can be written in the conservation form as

$$\frac{\partial\hat{U}}{\partial t}+\frac{\partial\hat{F}}{\partial\xi}+\frac{\partial\hat{G}}{\partial\eta}=\hat{S} \tag{C.13}$$

where

$$\hat{U}=JU$$
$$\hat{F}=J\left(F\xi_x+G\xi_y\right)$$
$$\hat{G}=J\left(F\eta_x+G\eta_y\right)$$
$$\hat{S}=JS$$

APPENDIX D

SOLUTION APPROACH

The Van Leer flux vector splitting scheme is applied to split the flux vector in the generalized Euler equations into forward and backward components, which have characteristic velocities in forward and backward directions, respectively, written as

$$\hat{F}\left(\hat{U}\right)=\hat{F}^{+}\left(\hat{U}\right)+\hat{F}^{-}\left(\hat{U}\right) \tag{D.1}$$

The monotone upstream-centered scheme for conservation laws (MUSCL) is then used to discretize the spatial derivative of the flux vector, given by

$$\frac{\partial\hat{F}\left(\hat{U}\right)}{\partial\xi}=\frac{\partial\hat{F}^{+}\left(\hat{U}\right)}{\partial\xi}+\frac{\partial\hat{F}^{-}\left(\hat{U}\right)}{\partial\xi} \tag{D.2}$$

where

$$\left(\frac{\partial\hat{F}^{+}\left(\hat{U}\right)}{\partial\xi}\right)_{i,j}=\frac{1}{\Delta\xi}\left(\hat{F}^{+}\left(\hat{U}^{-}_{i+1/2,j}\right)-\hat{F}^{+}\left(\hat{U}^{-}_{i-1/2,j}\right)\right) \tag{D.3a}$$

$$\left(\frac{\partial\hat{F}^{-}\left(\hat{U}\right)}{\partial\xi}\right)_{i,j}=\frac{1}{\Delta\xi}\left(\hat{F}^{-}\left(\hat{U}^{+}_{i+1/2,j}\right)-\hat{F}^{-}\left(\hat{U}^{+}_{i-1/2,j}\right)\right) \tag{D.3b}$$

Substituting Equations (D.3a) and (D.3b) into Equation (D.2), the approximation of spatial derivatives of the flux vector is given by

$$\left(\frac{\partial\hat{F}\left(\hat{U}\right)}{\partial\xi}\right)_{i,j}=\frac{1}{\Delta\xi}\left[\hat{F}^{+}\left(\hat{U}^{-}_{i+1/2,j}\right)-\hat{F}^{+}\left(\hat{U}^{-}_{i-1/2,j}\right)+\hat{F}^{-}\left(\hat{U}^{+}_{i+1/2,j}\right)-\hat{F}^{-}\left(\hat{U}^{+}_{i-1/2,j}\right)\right] \tag{D.4}$$

The notation $\hat{F}^{\pm}\left(\hat{U}^{\mu}\right)$ denotes $\hat{F}^{\pm}$ evaluated at $\hat{U}^{\mu}$. $\hat{U}^{\mu}$ is given by

$$\hat{U}^{-}_{i+1/2,j} = \hat{U}_{i,j} + \left\{s/4\left[(1-ks)\Delta_{-} + (1+ks)\Delta_{+}\right]\right\}_{i,j} \tag{D.5a}$$

$$\hat{U}^{-}_{i-1/2,j} = \hat{U}_{i-1,j} + \left\{s/4\left[(1-ks)\Delta_{-} + (1+ks)\Delta_{+}\right]\right\}_{i-1,j} \tag{D.5b}$$

$$\hat{U}^{+}_{i+1/2,j} = \hat{U}_{i+1,j} - \left\{s/4\left[(1-ks)\Delta_{+} + (1+ks)\Delta_{-}\right]\right\}_{i+1,j} \tag{D.5c}$$

$$\hat{U}^{+}_{i-1/2,j} = \hat{U}_{i,j} - \left\{s/4\left[(1-ks)\Delta_{+} + (1+ks)\Delta_{-}\right]\right\}_{i,j} \tag{D.5d}$$

where

$$\left(\Delta_{+}\right)_{i,j} = \hat{U}_{i+1,j} - \hat{U}_{i,j}$$
$$\left(\Delta_{-}\right)_{i,j} = \hat{U}_{i,j} - \hat{U}_{i-1,j}$$

The spatial differencing is second order central difference scheme when $k = 1$. s is the limiter, which governs the accuracy of the approximation. The limiter is introduced to locate regions where the solution is discontinuous, such as shock waves, and is required to eliminate oscillations in those regions, and is given by

$$s = \frac{2\Delta_{+}\Delta_{-} + \varepsilon}{\left(\Delta_{+}\right)^2 + \left(\Delta_{-}\right)^2 + \varepsilon} \tag{D.6}$$

where ε is a small number ($\varepsilon = 10^{-6}$) preventing division by zero in regions of null gradients.

Recall that the Van Leer flux vector splitting scheme in general 2-D coordinates is given by

$$\hat{F}^{+} = \hat{F}, \quad \hat{F}^{-} = 0 \quad for \quad M_{\xi} \geq 1 \tag{D.7a}$$

$$\hat{F}^{+} = 0, \quad \hat{F}^{-} = \hat{F} \quad for \quad M_{\xi} \leq -1 \tag{D.7b}$$

$$\hat{F}^{\pm} = J\sqrt{\xi_x^2+\xi_y^2}\begin{Bmatrix} e_1^{\pm} \\ e_1^{\pm}\left[\dfrac{\xi_x}{\gamma\sqrt{\xi_x^2+\xi_y^2}}\left(-\bar{u}_x \pm 2a\right)+u_x\right] \\ e_1^{\pm}\left[\dfrac{\xi_y}{\gamma\sqrt{\xi_x^2+\xi_y^2}}\left(-\bar{u}_x \pm 2a\right)+u_y\right] \\ e_1^{\pm}\left[\dfrac{-(\gamma-1)\bar{u}_x{}^2 \pm 2(\gamma-1)a\bar{u}_x + 2a^2}{\left(\gamma^2-1\right)}+\dfrac{u_x^2+u_y^2}{2}\right] \end{Bmatrix} \quad for \quad -1 < M_\xi < 1 \qquad \text{(D.7c)}$$

where

$$M_\xi = \frac{\xi_x u_x + \xi_y u_y}{a\sqrt{\xi_x^2+\xi_y^2}}$$

$$e_1^{\pm} = \pm\frac{1}{4}\rho a\left(M_\xi \pm 1\right)^2$$

$$\bar{u}_x = \frac{\xi_x u_x + \xi_y u_y}{\sqrt{\xi_x^2+\xi_y^2}}$$

Recalling Equation (D.4), the flux vector components $\hat{F}^+$ and $\hat{F}^-$ in Equations (D.7a)-(D.7c) are evaluated at $\hat{U}^{\mu}_{i\pm1/2,j}$, when calculate the spatial derivatives at grid point (*i*, *j*). $\hat{U}^{\mu}_{i\pm1/2,j}$ are obtained from Equations (D.5a)-(D.5d), in which $\hat{U}_{i-1,j}, \hat{U}_{i,j}$ and $\hat{U}_{i+1,j}$ are applied. Therefore, the metrics (ξ_x and ξ_y) in Equation (D.7c) are evaluated at the corresponding grid points, such as (*i*-1, *j*), (*i*, *j*) and (*i*+1, *j*). Similarly, the spatial derivatives in η direction can be obtained.

For the 2-D physical problem of a blast wave impacting a free-standing V-shaped or a free-standing cone-shaped structure, the physical domain in the front and in the back of the structure vary with time in *y* direction, but keep unchanged in *x* direction., due to the receding motion of the structure. The displacement of the structure is obtained through

$$y_p^{n+1} = y_p^n + u_p^* \Delta t \tag{D.8}$$

where y_p^{n+1} and y_p^n are the displacement of the structure at the time step n+1 and n, respectively. u_p^* is the velocity of the structure at the intermediate time step.

Linear interpolation is used to update the solution vector $\hat{U}$ in the transformed Euler equations for the different grid points and different time steps. The solution vector $\hat{U}$ at grid point (i, j) and time step n+1 is given by

$$\hat{U}_{i,j}^{n+1} = \hat{U}_{i,j}^n + \frac{\hat{U}_{i,j+1}^n - \hat{U}_{i,j}^n}{\Delta\eta}\left(\Delta y_{i,j}\right) \tag{D.9}$$

where $\Delta y_{i,j}$ is the moving distance of the grid point (i, j) between the time step n and n+1.